# A Global Dilepton Analysis in the $e\mu$ Channel Using 3.0 $fb^{-1}$ of CDF Data

M. Stephen M. Smith

Department of Physics, Duke University

Undergraduate Thesis

Spring 2009

Thesis Committee:

Mark Kruse, Ph.D. (Adviser)

Seog Oh, Ph.D.

Ronen Plesser, Ph.D.

Haiyan Gao, Ph.D.

# Abstract

In this analysis, we study the production of Standard Model processes from $p\bar{p}$ collisions at $\sqrt{s}$=1.96 TeV in the CDF II detector at Fermilab, in particular the content of the high $p_T$ dilepton events. The main processes considered are $t\bar{t}$, $WW$ and $Z \to \tau\tau$ while the background processes are $W+jets$, $W\gamma$, $WZ$, $ZZ$, $Z/\gamma* \to ee$, $Z/\gamma* \to \mu\mu$. In the final state of these processes, we require an electron and muon dilepton pair, and the other objects we expect to exist are neutrinos, which give our $\not\!\!E_T$ (Missing Transverse Energy) variable, and jets, from hadronizing quarks.

Therefore, we plot these events in two 2-D phase spaces $\not\!\!E_T$ vs. $N_{jets}$ and the $\not\!\!E_T$ vs. $\sum E_T$(jets), which provide a nice separation of our main processes. We are then able to fit our Monte Carlo simulated events to the data and extract the $t\bar{t}$, $WW$ and $Z \to \tau\tau$ cross sections, as well as develop a quantitative likelihood for the consistency of the data to the SM hypothesis in this parameter space.

In using this method for the extraction of cross sections, our measurements using 3.0fb$^{-1}$ of $e\mu$ data are: $\sigma_{t\bar{t}} = 8.20^{+1.17}_{-1.07}$ pb, $\sigma_{WW} = 12.28^{+2.05}_{-1.87}$ pb, and $\sigma_{Z\to\tau\tau} = 1513^{+173}_{-159}$ pb.

The results of quantifying the consistency of the data to the SM hypothesis yield no significant deviations from SM expectations. Although not done in this iteration of the analysis, this technique could also be used to search for specific new physics dilepton signatures.

# Acknowledgments

First and foremost I would like to thank my adviser Mark Kruse for giving me the chance to learn so much not only in the field of high energy physics, but also in many other areas of physics, computer programming, and presentation of my work. Thanks for the opportunities and lessons you have provided, which have prepared me for graduate school and beyond.

I would like to thanks Dean Andrew Hidas, (recently awarded) Ph.D., for all the time and support he gave me as well as for putting up with all my questions that flooded his e-mail inbox. I couldn't have asked for a more knowledgeable, patient mentor and friend as I learned the ropes of HEP and all of the jargon that goes with it. And I'm going to UCSD! Just like you in reverse.

Thanks to all my professors, who taught me so much over the last four years. In particular, thank you to Seog Oh and Ronen Plesser for helping me in the last couple, formative years to bring together my knowledge of physics and decide where to go next.

Lastly, I would like to thank my friends and family for supporting my endeavors in college and physics. Thanks Mom and Dad for everything you have given me–I could not ask for better parents. Alison Noel Dorsey, you have been a great friend, and I appreciate you always being there. Thanks everyone!

# Contents

# 1 Fundamental Particles of the Standard Model

This chapter discusses the constituents of the Standard Model of Particle Physics, which since its inception in the early 1960's has aptly described the observed most elementary particles of nature and the interactions among them (with the exception of the Higgs boson, which has yet to be discovered). Fermions and bosons are the two main classifications of particles described by the Standard Model. Fermions are spin-1/2 particles and comprise normal matter while bosons have integer spin and are mediators of the strong and electroweak forces.

## 1.1 Fermions

The spin-1/2 fermion particles are further composed of two different types: quarks and leptons. Hadrons are bound states of quarks, and hadrons of 2 or 3 quarks are called mesons and baryons respectively. Quarks interact through the strong and electroweak forces (see section on bosons) while leptons only interact through the electroweak force.

### 1.1.1 Quarks

The six types of quarks are up, down, charm, strange, top, and bottom. Each of these quarks has an anti-quark partner and two color partners. Quarks have non-integer electric charge and also a color charge, which is similar to electric charge but comes in the varieties of red, blue, and green. Also, another distinguishing characteristic of each quark is the quantum number associated with each, which is either positive or negative one. See Table 1 for a listing of these particle and their properties.

The quarks most familiar in everyday matter are the up and down quarks, which comprise protons and neutrons, and are therefore the first generation quarks. The second and third generation quarks are heavier and much more rare, usually only

| | Flavor | Charge ($q$) | Quantum Numbers | Mass (GeV) |
|---|---|---|---|---|
| First Generation | $u$ | +2/3 | U = +1 | (1.5 - 3.3) $\times 10^{-3}$ |
| | $d$ | -1/3 | D = -1 | (3.5 - 6.0) $\times 10^{-3}$ |
| Second Generation | $c$ | +2/3 | C = +1 | $1.27^{+0.07}_{-0.11}$ |
| | $s$ | -1/3 | S = -1 | $104^{+26}_{-34} \times 10^{-3}$ |
| Third Generation | $t$ | +2/3 | T = +1 | $171.2 \pm 2.1$ |
| | $b$ | -1/3 | B = -1 | $4.2^{+0.17}_{-0.07}$ |

Table 1: Properties of Quarks [1]

produced in high energy collisions such as in the experiment described in this analysis.

### 1.1.2 Leptons

The six lepton types described by the Standard Model are the electron, muon, tau, and the respective neutrino associated with each of these. Each of theses particles also has an anti-particle. We classify leptons by their electric charge and their lepton quantum numbers (see Table 2). The neutrinos in this table are listed as having an upper limit mass; however, measurements from neutrino mixing give strong evidence to the fact that neutrinos do have mass. Unlike quarks, leptons are colorless and are not subject to the strong force.

| Flavor | Charge ($q$) | Quantum Numbers | Mass (GeV) |
|---|---|---|---|
| $e$ | -1 | $L_e = 1$ | 0.511 $\times 10^{-3}$ |
| $\nu_e$ | 0 | $L_e = 1$ | $< 225 \times 10^{-9}$ |
| $\mu$ | -1 | $L_\mu = 1$ | 105.7 $\times 10^{-3}$ |
| $\nu_\mu$ | 0 | $L_\mu = 1$ | $< 0.19 \times 10^{-3}$ |
| $\tau$ | -1 | $L_\tau = 1$ | 1.777 |
| $\nu_\tau$ | 0 | $L_\tau = 1$ | $< 18.2 \times 10^{-3}$ |

Table 2: Properties of Leptons [1]

## 1.2 Bosons (Force Mediators)

Bosons, which are spin-1 particles (except for theorized graviton with spin-2), mediate all Standard Model interactions. The gluon ($g$) mediates the strong force and is a massless, bi-colored particle. The photon ($\gamma$), $W^{\pm}$, and $Z$ are the force carriers for the electroweak interactions. $W^{\pm}$ and $Z$ are massive particles while the photon is massless. The forces between quarks arrise from either strong or electroweak interactions while the forces between leptons arise only as a consequence of the electroweak interaction. Table 3 describes the four bosons.

| | Charge ($q$) | Interactions | Mass (GeV) |
|---|---|---|---|
| $g$ | 0 | strong | 0 |
| $\gamma$ | 0 | electromagnetic | 0 |
| $Z$ | 0 | weak | $91.1876 \pm 0.0021$ |
| $W^{\pm}$ | $\pm 1$ | weak | $80.398 \pm 0.025$ |

Table 3: Properties of Bosons [1]

# 2 Standard Model Processes Used in Analysis

In this section, we describe the processes we use in this analysis, for which we require an $e\mu$ dilepton final state. We consider the processes as coming from $q\bar{q}$ annihilation, due to the interactions of the constituent quarks in the $p\bar{p}$ collisions with center of mass energy $\sqrt{s}$=1.96 TeV at the Tevatron.

The "signal" processes for this analysis are $t\bar{t}$, $WW$, and $Z \rightarrow \tau\tau$. The decay modes for these processes that we consider are $t\bar{t} \rightarrow WbWb \rightarrow l\nu bl\nu b$, $WW \rightarrow l\nu l\nu$, and $Z \rightarrow \tau\tau \rightarrow l\nu_l\nu_\tau l\nu_l\nu_\tau$ ($l = e$ or $\mu$). Our "background" processes for this anaylsis that also contribute to our dataset are $W\gamma$, $WZ$, $ZZ$, $W$+jets, and $Z \rightarrow ee/\mu\mu$.

## 2.1 The $t\bar{t}$ Production and Decay

The $t\bar{t}$ process is one of the main contributions we expect to have a final state with electrons and muons. Figure 1 shows the leading order Feynman diagram for this process. We expect that approximately 85% of all $t\bar{t}$ production will occur in this way, that is through $q\bar{q}$ annihilation. The other 15% of production can be accounted for through $gg$ fusion. However, there are large uncertainties on these numbers; for example, at the Tevatron, $gg$ fusion production can vary from 10-20% (from theoretical predictions).

Branching ratios describe how often we expect a given process to decay in a certain mode. The $t\bar{t}$ events decay to $W^+bW^-\bar{b}$. The $W$ bosons then decay either leptonically or hadronically. We are interested in events where the $W$ bosons decay leptonically, specifically when one decays to an electron and the other decays to a muon. We are not interested in $\tau$ leptons as they also subsequently decay in various ways making their identification difficult. It is expected that the $W$ boson will decay to a lepton and neutrino $W^\pm \rightarrow l^\pm\nu$ (where $l$ indicates each type of lepton and not the sum over them)

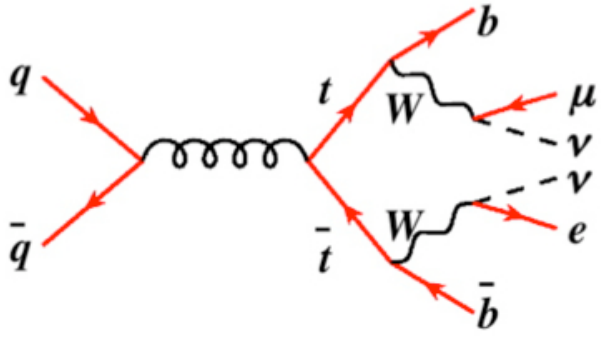


Figure 1: Leading Order Feynman Diagram for the $t\bar{t}$ process

with approximately a $\frac{1}{9}$ probability. Therefore, if we ultimately require an $e\mu$ dilepton final state, the branching ratio for this decay mode $t\bar{t} \rightarrow e\nu b\mu\nu\bar{b}$ is $\frac{2}{81}$. Despite the fact that this is a fairly low percentage, meaning fewer expected events for study, there are relatively few SM processes with an $e\mu$ final state having nice separation between the main processes in the parameter space of the variables we plot. This allows a relatively precise measurement of the $t\bar{t}$ production cross section. The $t\bar{t}$ cross section has a theoretical value $\sigma_{t\bar{t}} = 6.7 \pm 0.3$ pb [6].

## 2.2 The $WW$ Production and Decay

Another one of the main contributing processes is $WW$. The Feynman diagram for this process is shown in Figure 2, and we again expect that the percentage for $W \rightarrow e\nu$ or $W \rightarrow \mu\nu$ to be approximately $\frac{1}{9}$, and therefore the branching ratio for the decay mode to an $e\mu$ dilepton final state $WW \rightarrow e\nu\mu\nu$ is $\frac{2}{81}$. The next to leading order (NLO) predction for the $WW$ production cross section is $\sigma_{WW} = 12.4 \pm 0.8$ pb [6]. Since the cross sectionis greater for $WW$ than it is for $t\bar{t}$, we expect more events after the selection of an electron and muon.

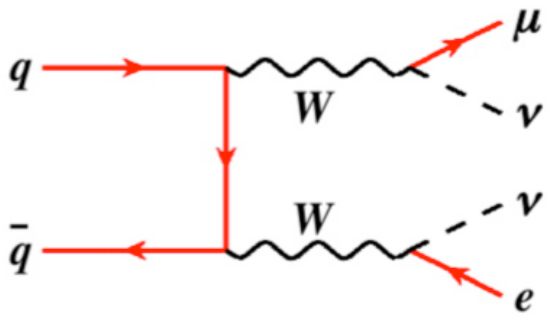


Figure 2: Leading Order Feynman Diagram for the $WW$ process

## 2.3 Drell-Yan ($Z \rightarrow \tau\tau$) Processes

The leading order Feynman diagram for the $Z \rightarrow \tau\tau$ through $q\bar{q}$ annihilation is shown in figure 3. The branching ratio for $Z \rightarrow \tau^+\tau^-$ is approximately 3.37 % while the branching ratio for both decay modes $\tau^- \rightarrow \mu^-\bar{\nu}_\mu\nu_\tau$ and $\tau^- \rightarrow e^-\bar{\nu}_e\nu_\tau$ is approximately 17.61 %. The same branching ratios apply to the $\tau^+$ leptons, which have similar but charge conjugate decay modes. Therefore we expect that $Z \rightarrow \tau^\pm\tau^\mp \rightarrow e^\pm\bar{\nu}_e\nu_\tau\mu^\mp\bar{\nu}_\mu\nu_\tau$ to occur about 0.59 % of the time. Despite the low percentage of this decay mode, the theoretical cross section for our $Z \rightarrow \tau\tau$ sample is quite large, measured in the PYTHIA Monte Carlo generator to be $\sigma_{Z\rightarrow\tau\tau} = 1780.8$ pb [7]. This cross section is for an invariant mass cut of 10 GeV, with a significant fraction of the $Z/\gamma* \rightarrow \tau\tau$ cross section to the the low mass of $\gamma*$ particles.

## 2.4 Background Processes

The background processes used in this analysis are $W+jets$, $W\gamma$, $WZ$, $ZZ$, $Z/\gamma* \rightarrow ee$, $Z/\gamma* \rightarrow \mu\mu$ and have leading order Feynman diagrams that can be drawn as arising from a quark and anti-quark pair. In particular, it should be noted that our largest background contribution, $Z/\gamma* \rightarrow \mu\mu$ contributes a fairly large number of events to our analysis since it has a large cross-section of 355 pb with a muon identified as an

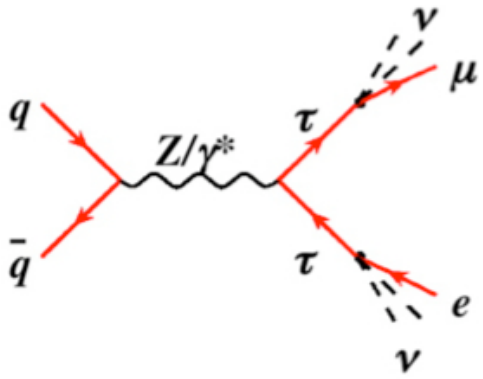


Figure 3: Leading Order Feynman Diagram for the $Z \rightarrow \tau\tau$ process

electron by the detector.

# 3 The Experimental Setup

In this analysis, we investigate high-energy collisions between protons and anti-protons ($p$ and $\bar{p}$), which are accelerated in the Fermilab Tevatron to a colliding center of mass energy of 1.96 TeV. One collision point on the Tevatron is at at the CDF II detector, which is used to investigate the decays and products of these collisions.

## 3.1 The Fermilab Tevatron

The Fermilab Tevatron is currently the highest energy (operational) hadron collider in the world, and it accelerates protons and anti-protons using eight different accelerators, which will be described in the next sections. A diagram of the chain of accelerators is shown in Figure 4.

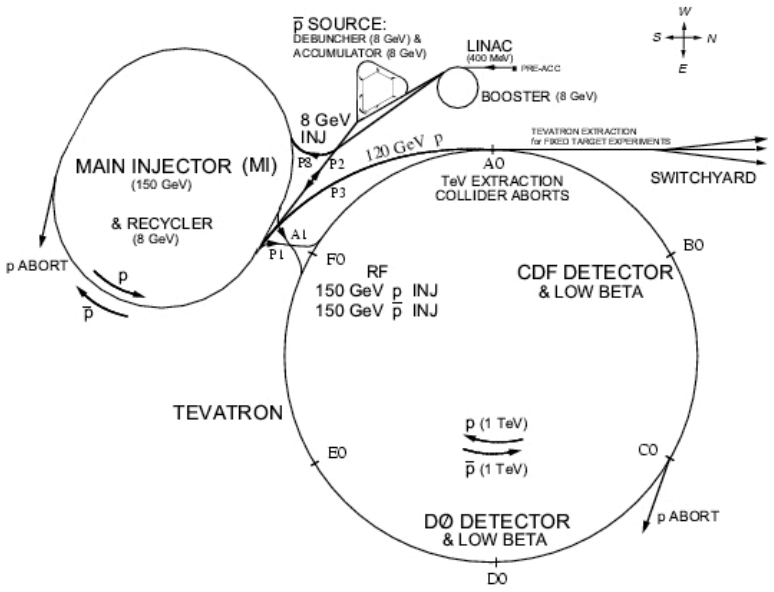


Figure 4: The Fermilab Tevatron Accelerating Chain [8].

### 3.1.1 Cockcroft-Walton

The Cockcroft-Walton is a Van de Graff accelerator that provides a continuous beam of $H^-$ ions (which begin as a gas) at 750 keV. This gas is placed in an electric field, which subsequently removes the electrons of the hydrogen atoms so that they become $H^+$ ions. Subsequently, the positive ions are attracted to a cesium anode, from which they acquire electrons, then are repelled from the anode, and eventually accelerated by the Cockcroft-Walton to 750 keV and sent to the Linac.

### 3.1.2 The Linac

The purpose of this accelerator is to create a beam of bunched $H^-$ ions in the linac. This is done by varying an electric field at a high frequency while ions are accelerated by these fields through successive drift tubes of increasing length. Due to the varying field, some negative ions are accelerated while others arrive at the Linac out of phase and are therefore decelerated. The ions that do make it through are bunched into a beam, and each bunch is accelerated to 400 MeV. At the end of the linac accelerator, the $H^-$ ions are pass through a thin carbon foil, which strip the electrons from the negative ions to give protons.

### 3.1.3 Booster

This sychrotron accelerates the bunches of protons to an energy of 8 GeV through 16,000 revolutions, where each revolution is about 475 m. The average increase of energy for the protons is 475 keV per revolution.

### 3.1.4 Main Injector

The main injector takes both protons and anti-protons (see next section) at 8 GeV. This is also a synchrotron which accelerate protons to either 120 GeV for production

of anti-protons or accelerate protons and anti-protons to 150 GeV for injection into the Tevatron ring.

### 3.1.5 Anti-Protons

Protons at 120 GeV from the main injector collide with a nickel target, which creates many different particles, a few of which are anti-protons. These particles are focused using a lithium lens, and the anti-protons are separated using a magnetic field. Anti-protons are only accumulated on the order of tens of mA per hour, a rate which only produces about 20 picograms of anti-protons every six years.

### 3.1.6 Debuncher, Accumulator, and Recycler

The anti-protons enter the debuncher at very high speeds and with a very large energy spread. The debuncher stochastically cools the beam of anti-protons so that the large energy spread lessens, creating a large time spread where the anti-protons have a more uniform energy distribution. These anti-protons are then sent to the accumulator, a 8 GeV storage ring used to collect successive injections from the debuncher. When the accumulator has enough anti-protons, the anti-protons are transferred to the recycler, which is a storage ring of permanent magnets at 8 GeV. Anti-protons are sent to the main injector from here before the Tevatron.

### 3.1.7 Tevatron

The Tevatron, which is roughly four miles in circumference with a little over 1000 superconducting dipole magnets, can accelerate protons and anti-protons to a center of mass energy of 1.96 TeV. Proton and anti-proton bunches come from the main injector, and the proton bunches circulate clockwise while the anti-proton bunches circulate counter-clockwise as viewed from above. There are 36 bunches of protons ($\sim 10^{11}$ protons) and

36 bunches of anti-protons ($\sim 10^{10}$ anti-protons) at any given time during operation.

These bunches are squeezed by the magnets to form tighter beams, have the excess particles around the beam removed, and made to collide at the center of the detector. The instantaneous luminosity for these collisions can be written as

$$\mathcal{L}_{inst} = fn\frac{N_p N_{\bar{p}}}{4\pi\sigma_x\sigma_y} \tag{1}$$

where $f$ is the frequency of revolution, $n$ is the number of bunches, $N_p$ and $N_{\bar{p}}$ the number of protons or anti-protons per bunch, and $\sigma_{x,y}$ the Gaussian beam profiles in the transverse direction. Luminosity can be thought of as the available area for interactions to occur, and multiplied by the cross section for a particular process, we can obtain a rate at which that process will occur.

## 3.2 The CDF Run II Detector

The CDF II Detector is located at the B0 interaction point on the Tevatron ring, and it consists of four layers used to measure of particles transversing through them. A schematic of the detector is shown in Figure 5. The layers nearest to the beam line are the tracking detectors (inside of magnets) and are used to reconstruct the momentum of charged particles. Outside of the detectors are the calorimeters, which measure the energy of particles that interact and deposit energy within them. The outermost layers are the muons chambers, which identify particles that pass through all other layers of the detector. Because so much data passes through the detector at a time, it is not possible to record all of this data, so an online hardware triggering system is used to look at some of the data for each event and decide whether to store it.

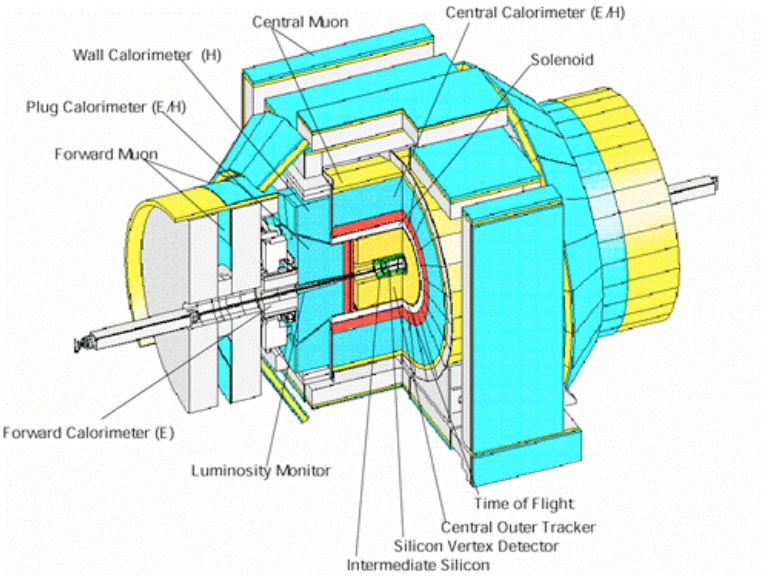


Figure 5: The CDF II Detector [8].

### 3.2.1 The CDF II Coordinate System

The CDF coordinate system is right handed, where the z-direction is the direction of the proton beam at the nominal ($z_0$) collision point. The positive y-direction is defined as pointing vertically upward while the x-direction points outward from the beam line.

An important kinematic variable to consider is rapidity, defined as

$$Y = \frac{1}{2}\ln\left(\frac{\mathrm{E}+\mathrm{p_z}}{\mathrm{E}-\mathrm{p_z}}\right) \tag{2}$$

and pseudo-rapidity ($\eta$) is a massless approximation of this quantity, which works well for particles considered in this analysis. By setting the energy and momentum equal to one another, we can define the pseudo-rapidity as

$$\eta = -\ln\left(\tan\frac{\theta}{2}\right) \tag{3}$$

where $\theta$ is the angle measured from the z-axis, a useful quantity to measure particles

in high energy experiments. The detector pseudo-rapidity ($\eta_{det}$), is used to define the pseudo-rapidity from the interaction point $z_0$ of the detector.

Other important coordinate aspect to note is $\Delta R$, which is defined as

$$\Delta R = \sqrt{\Delta\eta^2 + \Delta y^2} \tag{4}$$

used to specify objects within a cone of radius R around some reconstructed track.

### 3.2.2 The Tracking System

The two types of inner tracking detectors in the CDF II detector are the Silicon Tracker and the Central Outer Tracker (COT). Three major components comprise the silicon tracker, and they are the L00, SVX11, and the ISL. L00 (Layer Zero Zero) is a micro-strip detector mounted on the beam pipe at a radius of 1.1 cm. The next layer, SVXII consists of 5 layers of micro-strip that extend from a radius of 2.44 cm. to 10.6 cm. The intermediate silicon layers (ISL) extend from 20 to 30 cm. We use the silicon tracker in this analysis for two reasons. The first is to identify high momentum tracks in the forward region of the detector, in the range $1 < \eta < 2$. Also, the silicon layers are used to identify jets that do not come from the primary interaction point, but occur so close to it that the COT system can not determine the displacement.

The central outer tracker (COT) consists of 96 layers, covering a radial region from 40 to 137 cm. These layers are broken into 8 alternating axial and stereo super-layers, which are further divided into cells consisting of sense wires, potential wires, sharper wires, and field panels. Particle tracking is covered out to $|\eta_{det}| <1.1$.

The COT is filled with an Argon-Ethane gas mixture, which charged particles ionize as they pass through it. Free electrons are attracted to the sense wires after ionization, make contact with the sense wires, and cause a hit to be counted. By using the timing

information and hits on several wires, a track is reconstructed, from whose curvature momentum of the charged particle can be determined. The COT is useful is identifying high momentum track from muons, electrons, and jets. All central leptons are required to have a good quality track in the COT, and the COT is also used at the trigger level.

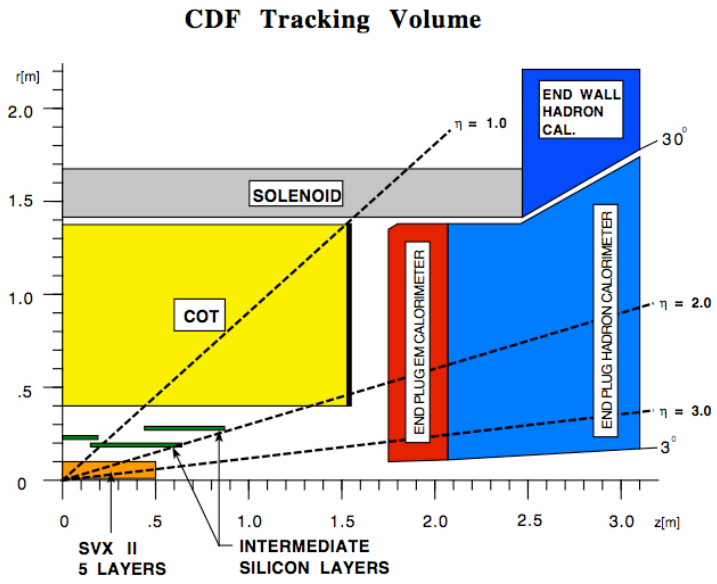


Figure 6: The CDF II Detector Tracking Volume [8].

### 3.2.3 Calorimetry

The calorimeters, consisting of layers of scintillator between layers of heavy metal, surround the tracking volume and measure the energy of particles that stop or pass through them. A shower of electrons and photons will be created when electrons and photons interact with the heavy metal, and hadrons will deposit energy in the calorimeters as well. Atoms in the scintillator excited by the showers of electron and photons emit photons as they return to the ground state, and these photons are amplified by photomultiplier tube. This signal's ampitude gives a measurement of the energy deposited.

The psedo-rapidity range covered by the central calorimeters is $0< |\eta_{det}| <1.1$ while the radial range is 173 to 347 cm. There are EM (electro-magnetic), HAD (hadronic), and shower-maximum detector (CES) portions. The EM calorimeter is where electrons and photons deposit most of their energy while the shower maximum part of the calorimeter measures the transverse shower profile to further assist in electron and photon identification. The hadronic calorimeter, located behind the EM calorimeter, consists of layers of steel and scintillator.

The plug calorimeter, also known as the forward calorimeter, covers a range of $1.1< |\eta_{det}| <3.6$ and likewise consists of an EM portion, a HAD portion, and a shower-maximum detector known as the PES.

### 3.2.4 The Muon Detection System

The CMU, CMP, and CMX muoon detectors used in this analysis are located in the outermost portions of CDF II detector. While many particles never make it to this level because they are stopped in the calorimetry portion, muons are minimally ionizing particles and will only deposit a small portion of their energy in the calorimeters. The muon detectors use drift chambers and scintillators to identify a charged particle which has passed through the entire detector. This is done by detecting the position of this particle and matching it to the track it left in the tracking detectors.

The CMU detector as well as the CMP detector (situated right outside of it) both cover a range of about $|\eta_{det}| <0.68$ while the CMX detector covers a more forward range of $0.65< |\eta_{det}| <1$.

### 3.2.5 Luminosity Measurement

The Cherenkov Luminosity Counter (CLC) is used to measure the instantaneous luminosity of the CDF II detector. Charged particles spread through the gas of two

meter long tubes, situated on either side of the detector at high $|\eta_{det}|$. Photons are given off by these particles and collected by photomultiplier tubes, which count hits. These hits along with knowing the inelastic $p\bar{p}$ cross section allow for the calculation of instantaneous luminosity, which has a total error of about 5.9 %.

### 3.2.6 Trigger System

The 3-level online trigger system is employed to pick out events that contain interesting properties and then to store those events. Level-1 triggers use basic calorimeter information, tracks from the COT that are reconstructed using the eXtremely Fast Tracker (XFT), and stubs reconstructed in the muon chambers in order to make a decision about an event. While the Level-1 triggers have only 5.5 microseconds to make a decision about storing an event, Level-2 triggers have 20 microseconds. Level-2 triggers also consider tracking information from the silicon detector and shower-maximum detectors. Level-3 triggers have two parts, which are the Event Builder (EB) and the L3 decision farm. The EB looks at raw detector output while the L3 farm makes decisions on higher level objects such as more sophisticated tracking. If the level-3 trigger identifies an event to keep, it is written to permanent storage.

# 4 Particle Identification

In this section, we define and describe the objects that will be used in this analysis. The fundamental components we need to identify are high-$p_T$ leptons (in particular electrons and muons), jets, and missing transverse energy ($\not\!\!E_T$). After defining what constitutes measuring a lepton in the CDF II Detector, we discuss the efficiencies for identifying a lepton in both simulation and data, and how we account for any descrepancies. Also, it should be noted that the lepton identification categories, efficiencies, and scale factors, used in this analysis were developed and measured in a $H \rightarrow WW$ analysis previously performed by the Duke HEP group [5] [3].

## 4.1 The Particle Traces in the Detector

The two lepton flavors, electrons ($e$) and muons ($\mu$), for this analysis are identified by how they are reconstructed in the CDF II detector. We use five categorizations in order to identify each lepton based on which detector components are used in the identification. Electron types are TCE and PHX while muon types are CMUP, CMX, and CMIOCES. A short description of these categories is given in Table 4. Later in this section, we will discuss the electron, muon, and track identification in more detail.

Also, a track isolation requirement on all lepton types other than PHX electrons is made. This isolation requirement is

$$\frac{\sum_{i \neq lepton}^{N} P_T^i}{P_T^{lepton}} < 0.1 \tag{5}$$

where N is the number of tracks within a cone o $\Delta R$ <0.4 of the lepton candidate track. We make this requirement in order to reduce the number of fake leptons accepted, and this requirement is satisfied by almost all leptons identified from $W$ and $Z$ boson

| | |
|---|---|
| **TCE** | Tight Central Electron: $\|\eta\|$ <1.1 |
| **PHX** | Forward Electron which relies on Silicon Tracking: 1.2< $\|\eta\|$ <2.0 |
| **CMUP** | Central Muon which has hits in both the CMU and CMP muon detectors: $\|\eta\|$ <0.6 |
| **CMX** | Muon which has hits in the CMX detector: 0.65< $\|\eta\|$ <1.0 |
| **CMIOCES** | Muon which does not satisfy the hit requirements of CMUP or CMX but is fully fiducial to the central calorimeter |

Table 4: Lepton categories used in this analysis with brief description of each.

| Event Selection Cuts |
|---|
| 2 high $P_T$ isolated leptons |
| Apply cosmic filter |
| Apply conversion filter |
| Require that the electron and muon be of opposite sign |

Table 5: Event selection cuts

decays [3].

## 4.2 Dilepton Event Selection

The data sample we use consists of isolated electrons and muons using the standard lepton cuts that are described above. In addition to these cuts, Table 5 describes the other event selection procedures.

### 4.2.1 Dilepton Categories

Events are classified by where in the detector the two leptons are found. We require that one lepton pass a muon trigger and that one lepton pass an electron trigger. Our data samples are reconstructed using only triggerable electrons from the central calorimeter (TCE) or tiggerable CMUP or CMX muons. Table 6 summarizes our

| Dilepton Type | Dilepton Category |
|---|---|
| $e\mu$ | TCE-CMUP |
| $e\mu$ | TCE-CMX |
| $e\mu$ | TCE-CMIOCES |
| $e\mu$ | PHX-CMUP |
| $e\mu$ | PHX-CMX |

Table 6: Dilepton Categories Used for This Analysis

dilepton types.

## 4.3 Electron Identification

When a high-$P_T$ electron enters the CDF detector, it is ultimately identified by the track it leaves as well as the energy it deposits in the calorimeter. An electron is expected to leave a track in both the silicon detector and the central outer tracker (COT). Also, because the electron has a relatively low mass and is electrically charged, most of its energy will be deposited in the EM calorimeter.

Electrons identified as Tight Central Electron (TCE) and forward (PHX) are used in this analysis. A central or TCE electron is identified in the $|\eta|$ <1.1 region of the detector while a PHX or forward electron is identified in the 1.1< $|\eta|$ <2.0 region of the detector. PHX electrons get there name from ehe PHOENIX algorithm that identifies forward electrons by matching plug EM calorimeter information to SVX hits. Table 4.3 gives the specific values of parameters used to select TCE and PHX electrons while these parameters are described below [3].

- **Region:** A flag that indicates if the electron track is fiducial to the central or plug calorimeters.

- **Fiducial:** For a TCE identification, the track must be fiducial to the CES.

| **Central Electrons (TCE)** | |
|---|---|
| Region | Central ($\|\eta\|$ <1.1) |
| Fiducial | Track fiducial to CES |
| Track $P_T$ | $\geq$ 10 or $\geq$ 5 if $E_T$ <20 (GeV) |
| Track $\|z_0\|$ | $\leq$60 cm. |
| # of Axial SL | $\geq$3 with $\geq$5 hits |
| # of Stereo SL | $\geq$2 with $\geq$5 hits |
| Conversion Flag | $\neq$1 |
| Isolation/$E_T$ | $\leq$ 0.1 |
| $E_{HAD}/E_{EM}$ | <0.055+0.00045 $\cdot$ E |
| $L_{shr}$ | $\leq$0.2 |
| $E/P$ | <0.055+0.00045$\cdot$ $E_t$ |
| CES $\Delta X$ | -3 $\leq$ q $\cdot$ $\Delta X$ $\leq$ 1.5 |

| **Forward Electrons (PHX)** | |
|---|---|
| Region | Plug (1.2< $\|\eta\|$ <2.0) |
| $\eta_{PES}$ | (1.2< $\|\eta\|$ <2.0) |
| $E_{HAD}/E_{EM}$ | <0.05 |
| PEM 3x3 Fit | true |
| $\chi^2_P ES$ | $\leq$ 10 |
| PES 5x9 U | $\geq$ 0.65 |
| PES 5x9 V | $\geq$ 0.65 |
| Isolation/$E_T$ | $\leq$ 0.1 |
| $\Delta R$(PES,PEM) | $\leq$3.0 |
| Track Method | true |
| # of Silicon Hits | $\geq$3 hits |
| Track $\|z_0\|$ | $\leq$60 cm. |

Table 7: Electron Identification Requirements

- **Track $z_0$:** The longitudinal (z) position of the track where it intersetcs the beamline.

- **Axial and Stereo SL:** The number of axial and stereo superlayers in the COT which have at least 5 hits associated with the track.

- **Conversion flag:** Identification of whether electrons come from a photon conversion

- **Isolation/$E_T$:** The energy deposited in the calorimeter within a cone of radius $\Delta R \leq 0.4$ around the electron cluster (or if muon, muon track) excluding the energy of the electron cluster (or if muon, deposited by the muon) divided by the $E_T$ ($P_T$) of the electron (or muon) candidate.

- **$E_{HAD}/E_{EM}$:** the ratio of the energy deposited in the hadronic part of the calorimeter to the energy deposited in the electromagnetic part of the calorimeter.

- **$L_{shr}$:** A variable that compares the lateral shower profile in towers next to the seed tower to an expected profile given by

$$L_{shr} = 0.14 \frac{\sum_i (M_i - P_i)}{\sqrt{(0.14\sqrt{E_{EM}})^2 + \sum_i (\Delta P_i)^2}} \tag{6}$$

  where $i$ denotes the adjacent towers, $M_i$ the measured energy, and $P_i$ the predicted energy in the $i$th tower.

- **$E/P$:** The ratio of energy measured in the calorimeter to the momentum calculated from the measurement of the track curvature.

- **CES $\Delta X$:** In the $r - \phi$ plane, this is the difference between the best CES match and the COT beam-constrained track extrapolation to the CES.

- $\eta_{PES}$**:** The pseudo-rapidity as measured by the best match PES cluster.
- **PEM 3x3 Fit:** A $\chi^2$ fit to electron test beam data of 9 PEM towers
- $\chi^2_{PES}$**:** A $\chi^2$ fit to electron test beam data for shower-maximum profile
- **PES 5x9 U/V:** The ratio of the central 5 tower energy to the total 9 tower energy
- $\Delta R$**(PES,PEM):** In the $r-\phi$ plane, this is the difference between the best PES match and the PEM match.
- **Track Matched:** PHX electrons must have a track that is matched to the PEM cluster and event vertex.
- **# of Silicon Hits:** The number of hits in the silicon detectro associated with specific track. The maximum number of hits is eight.

## 4.4 Muon Identification

Because muons are minimizing ionizing particles, they often traverse the entire CDF detector. Muons will deposit very little energy in the calorimeters through which they pass, but they will leave a track in the tracking chamber. Also, if they pass through the detector fiducial to the muon chambers, then they will leave a short track referred to as a stub.

The four muon categories used in the analysis are CMUP, CMX, and CMIOCES. These types are determined by the detector through which the muon passes. The detectors have differing efficiencies due to different locations, components, and geometry, and these efficiences are given in Section 3.2.

There are certain base requirements that all muons must fulfill, which are listed in Table 8. Also, muons are further designated by the specific detector through

which they pass. CMUP muons must have a stub in both the CMU detector as well as a track in the outer muon chambers. The pseudo-rapidity range accounted for is $\eta_{det}$ <0.68. CMX muons must have a stub in the CMX detector, which covers the range 0.68< $\eta_{det}$ <1. It is also possible to identify muons not fiducial to these detectors by identifying a high-$P_T$ track that points to a calorimeter with that of a minimizing ionizing particle, but this will not be discussed further. Cuts unique to muons (and were not discussed in the previous section) are explained below while the requirements for different muons types (in addition to the base cuts) are given in Table 9 [3].

- **CM(U|P|X)** $x_{fid}$**,** $z_{fid}$**:** The muon track must be must be fiducial to the specific detector it passes through, and for a CMX muon, the muon must be within 3 cm. in the $z_{fid}$ of the edge of the detector. The coordinates refer to the face of the muon detector and no the CDF II coordinate system.

- $\Delta X_{CM(U|P|X)}$**:** The distance between the track position to the specific detector and the actual muon stub in that detector.

- $\rho_{COT}$**:** The radius at which the track leaves the COT. This value is taken into account so that it is known that the muon is able to be triggered on by the CMX trigger track requirements.

- $d_0$**:** The distance of closest approach of the muon track to the beamline.

- $\chi^2$**:** This value compares the track to the hit information in the tracking detectors.

- **Curvature Significance:** The measured track curvature divided by the curvature error.

| | |
|---|---|
| $P_T$ | >10 GeV) |
| $E_{EM}$ | <2+max(0,($p$-100)·0.0115) |
| $E_{HAD}$ | <6+max(0,($p$-100)·0.028) |
| Isolation/$P_T$ | $\leq$0.1 |
| # of Axial SL | $\geq$3 with $\geq$5 hits |
| # of Stereo SL | $\geq$2 with $\geq$5 hits |
| Track $z_0$ | <60 cm. |
| Track $d_0$ | <0.2 cm. (<0.02 cm. with silicon) |
| $\chi^2/dof$ | <4.0 cm. (<3.0 cm. if Run>186598) |

Table 8: Identification requirements for all muon types.

| **CMUP Muon** | |
|---|---|
| CMU Fiducial | $x_{fid}$ <0,$z_{fid}$ <0 cm |
| CMP Fiducial | $x_{fid}$ <0,$z_{fid}$ <0 cm |
| $\Delta X_{CMU}$ | < 7cm |
| $\Delta X_{CMP}$ | $< max(6,150/P_T)$ cm |

| **CMX Muon** | |
|---|---|
| CMX Fiducial | $x_{fid}$ <0,$z_{fid}$ <0 cm |
| $\Delta X_{CMX}$ | $< max(6,125/P_T)$ cm |
| $\rho_{COT}$ | > 140 cm |

| **CMIOCES Muon** | |
|---|---|
| Uniqueness | Not a CMUP or CMX |
| $E_{EM} + E_{Had}$ | >0.1 GeV |
| # of Stereo SL | $\geq$2 with $\geq$5 hits |
| Fiducial | Track fiducial to PES |
| COT hit fraction | >0.6 |
| $\chi^2/dof$ | < 3.0 |

Table 9: Additional identification requirements for the three muon types used in this analysis.

## 4.5 Hadronic Jet Identification

In $p\bar{p}$ collisions, quarks and gluons can be the outcome of inelatic collisions between the proton and anti-proton as well as from intial state or final state radiation. Jets are the result of the hadronization of quarks. Hadronization of a quark or gluon is due quantum chromodynamics (QCD) confinement, which states that particles that carry a color charge can not exist in free form. Therefore, quarks fragment into hadrons, or bound states of quarks, before they are ever detected. In the CDF II detector, jets are identified by large energy deposits in both the hadronic and electromagnetic clusters as well as several closely assembled tracks that point to these calorimeters [3].

A jet is further characterized in the analysis by having a calorimeter cluster that is of size $\Delta R$ <0.4, a pseudo-rapidity of $|\eta|$ <2.5, and a total corrected transverse energy of $E_T$ >15 GeV. The raw detector energy for each jet is corrected for any non-linearity and energy loss in the uninstrumented regions of the calorimeter. Because identified electrons always satisfy the jet requirements, an object already identified as an electron and within a cone $\Delta R$ <0.4 will not be counted as a jet.

## 4.6 Neutrinos (Missing Transverse Energy, $\not\!\!E_T$)

Because neutrinos produced in the final state only interact with matter through the weak interaction, they do not leave a track in the detector or energy deposit in the calorimeters. Instead, they must be detected indirectly by looking at the energy imbalance they create in the detector. In the transverse plane of the detector, the plane that includes the interaction point and is perpendicular to the beam line, there should be an initial momentum of zero, since the colliding proton and anti-proton have equivalent mass and energy. Therefore, when the final momentum in the transverse plane is non-zero, this "missing" energy can be used to define the transverse missing energy.

We define the *raw* missing transverse energy ($\not\!\!E_T$) as

$$\vec{\not\!\!E_T}^{raw} = -\sum_i \vec{\not\!\!E_T}^{i} \tag{7}$$

where $\vec{\not\!\!E_T}^{i}$ is the transverse component of the energy in the $i$th calorimeter tower as defined at $z_0$=0. While this raw $\not\!\!E_T$ is used at the trigger level, at the analysis level we must correct for other sources of missing energy, the largest one being the $\not\!\!E_T$ contribution of the muons. Since the muons are minimum ionizing particles, they leave very little energy in the calorimeter, and most of their energy is carried out of the detector. In order to account for this, the momentum of the muon track is added back to the total momentum of the collision event and the small amount of energy identified as being left by the muons in the caolrimeter is subtracted. Another modification made to the $\not\!\!E_T$ accounts for the correction to the raw jet energies, discussed in the last section. Therefore, the real source of the $\not\!\!E_T$ in this analysis comes from neutrinos produced in electroweak interactions. The $\not\!\!E_T$ at the analysis level can be given by the equation

$$-\vec{\not\!\!E_T} = \sum_i \vec{E}_T^i + \sum_\mu \vec{P}_T^\mu - \sum_\mu \vec{E}_T^\mu(\text{Em} + \text{Had}) + \sum_{\text{j}} \vec{\text{E}}_{\text{T}}^{\text{j}}(\text{jet correction}) \tag{8}$$

where $E_T$ is corrected to be the actual energy in transverse plane, that is for the coordinate $z_0$, the z-coordinate of the interaction point on the beam line [3].

### 4.6.1 Event Triggers

The events used in this analysis must first pass one of three specific triggers before being added to our event total. The three trigger paths used in this analysis are ELECTRON-CENTRAL-18, MUON-CMUP-18, and MUON-CMX-18. Using a minimal amount of identification cuts, these triggers are designed to identify high-$P_T$ electrons and muons.

| Level 1 |
| --- |
| A central EM cluster with at least<br>$E_T > 8$ GeV<br>$E_{had}/E_{em} < 0.125$<br>At least one XFT track with $P_T$ >8.34 GeV |
| Level 2 |
| Additionally requires EM cluster with at least<br>$E_T$ >16 GeV<br>and in range $\|\eta_{det}\| < 1.317$ |
| Level 3 |
| Requires<br>$L_{shr}$ <0.4<br>$\Delta z$ <8 cm. between COT track and CES shower location<br>$E_T$ >18 GeV<br>COT track with $P_T$ >9 GeV<br>Track z-vertex is used, 3-tower EM cluster used. |

Table 10: CENTRAL-ELECTRON-18 Trigger Requirements

Tables 10, 11, and 12 give the specific requirements for the three triggers at each of the three trigger levels [4].

| Level 1 |
| --- |
| Requires<br>XFT track with $P_T > 4.09$ GeV<br>which is fiducial to the CMP and a CMP stub with track having $P_T$ >8.34 |
| Level 2 |
| Additionally requires<br>4-layer XFT track with $P_T$ >8.34 GeV<br>which is fiducial to both CMU and CMP detectors |
| Level 3<br>Requires<br>COT track with $P_T$ >18 GeV<br>Track extrapolation hits CMU and CMP detectors within $\Delta x_{CMP}$ <20 cm and $\Delta x_{CMU}$ <10 cm |

Table 11: MUON-CMUP-18 Trigger Requirements

| Level 1 |
| --- |
| Requires<br>Muon stub in CMX with $P_T$ >6 GeV<br>XFT track with $P_T$ >8.34 GeV<br>A hit in the CSX |
| Level 2 |
| Additionally requires<br>4-layer XFT track with $P_T$ >10.1 GeV |
| Level 3<br>Requires a COT track with $P_T$ >18 GeV<br>Muon stub in CMX within $\Delta x_{CMX}$ <10 cm |

Table 12: MUON-CMX-18 Trigger Requirements

### 4.6.2 Lepton ID Scale Factors

There is a known and different efficiency for identifying a object as a lepton in the data and in Monte Carlo simulations, which is called the ID efficiency ($\epsilon_{ID}$). The lepton ID scale factor is defined as

$$s_{lep} = \frac{\epsilon_{ID}^{data}}{\epsilon_{ID}^{MC}} \tag{9}$$

and is used to calculate the overall acceptance, which is discussed in Section 6.1. Table 13 gives the scale factors used in this analysis.

| Lepton Category | Period 0 | Period 1-4 | Period 5-7 | Period 8-10 |
|---|---|---|---|---|
| CMUP ID | 1.027 ± 0.011 | 0.995 ± 0.008 | 0.986 ± 0.010 | 0.991 ± 0.007 |
| CMUP Reco | 0.944 ± 0.007 | 0.936 ± 0.007 | 0.938 ± 0.009 | 0.956 ± 0.006 |
| CMX ID | 1.013 ± 0.014 | 0.985 ± 0.013 | 0.994 ± 0.016 | 1.002 ± 0.010 |
| CMX Reco | 1.013 ± 0.008 | 1.014 ± 0.010 | 1.014 ± 0.012 | 0.998 ± 0.010 |
| CMIOCES | 1.049 ± 0.019 | 1.050 ± 0.016 | 1.078 ± 0.019 | 1.046 ± 0.013 |
| TCE | 1.009 ± 0.006 | 0.994 ± 0.005 | 0.987 ± 0.007 | 0.974 ± 0.005 |
| PHXTrk | 0.999 ± 0.005 | 1.008 ± 0.004 | 1.016 ± 0.005 | 0.999 ± 0.003 |
| PHXPEM | 0.951 ± 0.006 | 0.953 ± 0.005 | 0.943 ± 0.006 | 0.931 ± 0.004 |

| Lepton Category | Period 11-12 | Period 13 | Period 14-17 |
|---|---|---|---|
| CMUP ID | 0.966 ± 0.008 | 0.975 ± 0.009 | 0.983 ± 0.007 |
| CMUP Reco | 0.940 ± 0.008 | 0.948 ± 0.008 | 0.925 ± 0.007 |
| CMX ID | 0.979 ± 0.014 | 0.998 ± 0.015 | 0.967 ± 0.014 |
| CMX Reco | 0.984 ± 0.013 | 0.992 ± 0.014 | 0.999 ± 0.014 |
| CMIOCES | 1.077 ± 0.016 | 1.073 ± 0.021 | 1.086 ± 0.014 |
| TCE | 0.964 ± 0.006 | 0.972 ± 0.007 | 0.981 ± 0.006 |
| PHXTrk | 0.995 ± 0.004 | 0.998 ± 0.005 | 1.024 ± 0.004 |
| PHXPEM | 0.938 ± 0.005 | 0.934 ± 0.006 | 0.943 ± 0.005 |

Table 13: Lepton ID Scale Factors for data periods 0-17, which are the actual scale factors applied to the Monte Carlo samples

# 5 Analysis Strategy

## 5.1 Motivation and Analysis Introduction

The purpose of this analysis is to gain a global understanding of the content of the high-$p_T$ dilepton events. We require that the dilepton final state be an $e\mu$ (electron and muon) pair with $p_T > 20$ GeV ($E_T > 20$ GeV) for each muon or electron. Considering the processes that meet this requirement in their final state, we look at what other objects can exist for each of the processes. The two possibilities we consider are neutrinos (which give $\not\!\!E_T$) and jets (hadronizing quarks, from final state decays or initial/final state QCD radiation). In order to compare the different processes, we create two-dimensional plots of $\not\!\!E_T$ vs. $N_{jets}$ (number of jets) and also $\not\!\!E_T$ vs. $\sum E_T$(jets) of Jets. In this way, we can compare our data to the expected Standard Model contributions. We are using both $N_{jets}$ and $\sum E_T$(jets) because the previous incarnation of the analysis used $N_{jets}$, but $\sum E_T$(jets) apperas to be better discriminated for our main processes. However, it should be noted they are highly correlated variables.

To quantify this comparison, we form a binned likelihood function, $L$, which is the product of the Poisson probabilities in each two-dimensional bin, with Gaussian terms to constrain the acceptances and luminosities within their systematic errors. Next, we fit the data to the expected $\not\!\!E_T$ vs. $N_{jets}$ and $\not\!\!E_T$ vs. $\sum E_T$(jets) templates in order to extract the main process cross sections of $t\bar{t}$, $WW$, and $Z \rightarrow \tau\tau$ using a maximum likelihood technique. Two sets of fits are performed. First, we allow the main processes to all "float", which means that they are free to take on any values during maximizing the likelihood $L$, thereby simultaneously extracting all three cross sections. This also gives us a global comparison of the Standard Model to the data in this $e\mu$ channel, which has the prospect of revealing new physics processes. Next, we Gaussian constrain (constrain within their uncertainties) all but one of the processes

to extract its cross section, which gives more precise cross section measurements of the individual processes.

One strength of the $\not\!\!E_T$ vs. $N_{jets}$ and the $\not\!\!E_T$ vs. $\sum E_T$(jets) plots is that they provide a nice separation in these phase spaces of the main contributing processes. Therefore, we can extract section measurements from these phase spaces and be fairly insensitive to uncertainties in the expected shapes. When this analysis was done previously using 360 $pb^{-1}$ of CDF data, only the phase space $\not\!\!E_T$ vs. $N_{jets}$ was used. By using the $\not\!\!E_T$ vs. $\sum E_T$(jets) phase space, we hope to create greater separation between the main processes and possibly a better measure of the main process cross sections. This is because the jets in the $t\bar{t}$ come from the high-$E_T$ b quarks in the final state while jet in $WW$ and $Z \rightarrow \tau\tau$ events come from the typically "softer" QCD radiation. Figure 7 shows this separation.

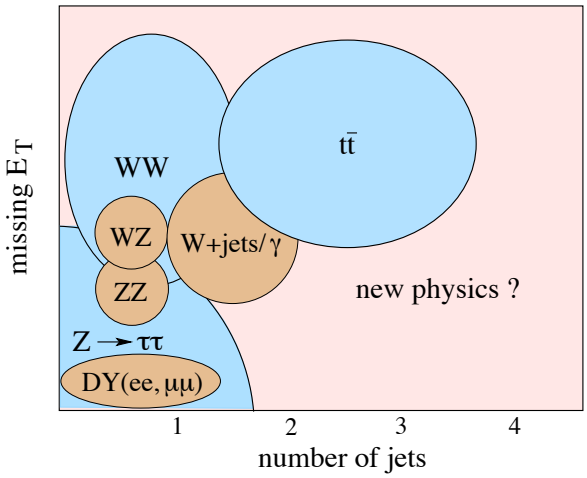


Figure 7: Schematic of Contributing Processes in the $\not\!\!E_T$ vs. $N_{jets}$ phase space

Another strength of this method is that no cuts (besides requiring high-$p_T$ $e\mu$ events) are made on the objects that we expect to be in the final state, namely neutrinos and jets. Instead, we fit the data to the two-dimensional phase spaces where our main processes are nicely separated, and we therefore keep more events than we would have

through making cuts. This allows us to utilize the full statistical power of the $e\mu$ sample, leading to more precise cross section extractions for the main processes $t\bar{t}$, $WW$, and $Z \rightarrow \tau\tau$.

## 5.2 $\not\!\!E_T$ and Jet Multiplicity Expectations in $e\mu$ final state

The following discussion of our three signal processes describes how the the two variables, $\not\!\!E_T$ and $N_{jets}/\sum E_T(\text{jets})$ create a separation in the two-dimensional phase space that allow us to globally extract the signal process cross sections.

1. $t\bar{t}$

   In the final state of each event for this process we expect two jets from $b$ quarks from the top decay. The jets can also come from the ISR and FSR, but this is more rare. The $\not\!\!E_T$ come from the leptonic decay of the $W$ boson where a neutrino accompanies the two leptons produced. Due to their different sources of production, the $\not\!\!E_T$ and jet multiplicity have very little correlation.

2. $WW$

   Since there are no quarks in the final state, the jets in this event come only from ISR and FSR, which implies a very small jet multiplicity. The $\not\!\!E_T$ comes from the two nuetrinos that are produced the $W$ boson decays. The $\not\!\!E_T$ is somewhat correlated with the jet multplicity.

3. $Z \rightarrow \tau\tau$

   From the leading order Feynman diagram, we expect there to be no jets since there are no final state quarks. The jets in the event therefore come only from ISR and FSR. Also, we expect almost no $\not\!\!E_T$ since the neutrinos produced from the tau decays tend to have back to back tranverse momentums, which essentially cancels their contribution to the $\not\!\!E_T$. However, if the $Z$ boson recoils of the ISR

neutrino, the directions of the netrinos are less aligned, and the $\not\!\!E_T$ noteably increases. This means a large correlation between the jet multiplicity and the $\not\!\!E_T$.

4. Background Contributions

   All the background contributions including $WZ$, $ZZ$, $W\gamma$, $Z/\gamma*$, and $W$+jets are expected to have a low number of jets, as they come mostly from ISR and FSR contributions.

### 5.2.1 Fake Leptons ($W + jet$)

A particularly difficult background to estimate is that due to $W + jet$ events where a lepton can be "faked" by a jet if that jet passes the selection criteria for one of the lepton types. This happens when a $W$ boson decays to a lepton and neutrino while the jet fakes a lepton. The probability of this occurring is quite low, however, and is difficult to measure with Monte Carlo programs and CDF II simulation, which can not correctly estimate the contribution of this background, and the measurement is instead data-based. First, we get the probability of a jet faking a lepton from four inclusive jet samples in the data, which have trigger requirements based on a leading jet $E_T$ of 20, 50, 70, and 100 GeV. We then apply these probabilities to the jets in the $W + jet$ sample, which in the final state is composed of leptons, $\not\!\!E_T$ from neutrinos, and jets.

# 6 Global Method for Measuring Standard Model Cross Sections

## 6.1 Monte Carlo Simulated Datasets

Many more events are produced in the Monte Carlo samples than the number of events we expect in the data for each process. This is due in part to the much higher integrated luminosity of the Monte Carlo samples, which we scale according to the integrated luminosity of our data, in this case $3.0 fb^{-1}$. We also must give a weight to each Monte Carlo event in order to accoutn for difference in lepton idetification, trigger, vertex, and filter efficiences. These efficiences multiplied gives us our acceptance, $A$. The weight of each Monte Carlo event is given as

$$w = \frac{\sigma \cdot \mathcal{B} \cdot \epsilon_{filter} \cdot \epsilon_{trig} \cdot s_{lepton} \cdot \epsilon_{vtx} \cdot \mathcal{L}}{N_{gen}} \tag{10}$$

where

- $\sigma$ is the cross section for a given process.
- $\mathcal{B}$ is the branching ratio for a given process.
- $\epsilon_{filter}$ is the filter efficiency for the specific Monte Carlo generator used.
- $\epsilon_{trig}$ is the trigger efficiency determined from the probability that the CDF II detector will trigger on a certain event in the data.
- $s_{lepton}$ is the scale factor for lepton ID effiencies (the ratio of $\epsilon_{ID}^{data}$ to $\epsilon_{ID}^{MC}$ as discussed previously).
- $\epsilon_{vtx}$ is the efficiency of the z-vertex cut $|z_{vtx}|$ <60 cm.

- $\mathcal{L}$ is the luminosity of the data used.

- $N_{gen}$ is the number of generated events in a given process Monte Carlo sample.

This weight is applied to each event in the generated Monte Carlo samples, and the sum of the weights of the events gives our final number of expected events for each process. Also, because $N_{exp} = \sigma \cdot A \cdot \mathcal{L}$, if the effiencies (and therefore the acceptance) for the data were the same as in the Monte Carlo, then the weight would reduce to $w = \frac{\int \mathcal{L}_{data} dt}{\int \mathcal{L}_{MC} dt}$ [3].

## 6.2 Good Run Lists and Luminosity Used

This analysis uses 3 $fb^{-1}$ of data from the CDF II detector. This data is divided into 17 data "periods", which occurred from February 4, 2002 to April 16, 2008. The lists that are kept of which data taking runs had certain components on an reliably working are known as "good run lists". The luminosity, or amount of data, associated with these good run lists as well as the lists themselves are given in Table 14. the uncertainty on the measurement of the luminosity of the detector is estimated to be 5.9%.

| Good run list | $\int \mathcal{L} dt$ ($\mathrm{pb}^{-1}$) |
|---|---|
| EM_NOSI | 2960.5 |
| EM_CMUP_NOSI | 2922.9 |
| EM_MU_NOSI_CMXIGNORED | 2829.5 |
| EM_SI | 2820.5 |
| EM_CMUP_SI | 2785.4 |
| EM_MU_SI_CMXIGNORED | 2695.4 |

Table 14: Luminosity corresponding to the different good run lists (v23) used in this analysis.

## 6.3 Monte Carlo Events

In order to have a comparison to our data, events are simulated through Monte Carlo generators in order to model our expected sample and background process contributions. In Table 15, our sample and background Monte Carlo processes are shown along with the generators used to generate them, the theoretical cross sections, and also the run-dependent periods they model. Most of the Monte Carlo samples are created through the PYTHIA generator with the exceptions of $WW$ through the MC@NLO generator, $W\gamma$ through the BAUR generator, and the $W + jet$ background, which is obtained through data (see Section 5.2.1).

The Monte Carlo is run dependent since the detector simulation is modelled in a time-dependent fashion, which accounts for changes in the detector as well as different instantaneous luminosity profiles of the detector during some period. Another aspect of Table 15 to note is the cross section used for each sample. For $t\bar{t}$, the listed cross section includes a specific branching ratio (here 0.1026) while $Z/\gamma*$ processes are multiplied by a "k-factor" (here 1.4), a number used to correctly estimate the number of events from these contributions.

| **Signal Process** | **Period** | **Cross Section (pb)** | **Generator** |
|---|---|---|---|
| $t\bar{t}$ | 0-11 | 6.7×0.1026 | PYTHIA |
| $WW$ | 0-7 | 12.4 | MC@NLO |
| $Z/\gamma* \rightarrow \tau\tau(M_{ll} >10)$ | 0-17 | 1272 × 1.4 | PYTHIA |
| **Background Process** | **Period** | **Cross Section (pb)** | **Generator** |
| $Z/\gamma* \rightarrow ee$ | 0-17 | 355 × 1.4 | PYTHIA |
| $Z/\gamma* \rightarrow \mu\mu$ | 0-17 | 355 × 1.4 | PYTHIA |
| $WZ$ | 0-17 | 3.65 | PYTHIA |
| $ZZ$ | 0-17 | 1.511 | PYTHIA |
| $W\gamma$ | 0-11 | 13.6 | BAUR |
| $W + fake\ lepton$ | 0-17 | – | Data |

Table 15: The signal and background samples used in this analysis with cross sections and data periods modelled, along with the generators used for Monte Carlo samples.

## 6.4 Maximum Likelihood

To measure the cross sections of $t\bar{t}$, $WW$, and $Z \to \tau\tau$, we use a maximum likelihood technique. We actually minimize the negative log-likelihood of the fit, but this is equivalent to maximizing the likelihood. The software used for the minimization is the from the MINUIT [9] package. As discussed previously, we extract the cross sections with the three main processes allowed to float in our fit as well as allowing only one of the main processes to float while the others are constrained within their Gaussian uncertainties. This is done using the $\not\!\!E_T$ vs. $N_{jets}$ templates and then repeated for the $\not\!\!E_T$ vs. $\sum E_T(\text{jets})$ templates.

The likelihood function is formed by taking the Poisson probabilities in each $i$-th bin of these templates where the Poisson probability is given by

$$P_i = \frac{\mu_i^{n_i} e^{-\mu_i}}{n_i!} \tag{11}$$

where $\mu_i$ is the expected number of events in bin $i$ while $n_i$ is the number of events observed in the data. In each bin, the expected number of events is calculated as

$$\mu_i = \sum_k \alpha_k \left[ \prod_j (1 + f_k^j S_j) \right] (N_k^{exp})_i \tag{12}$$

where $k$ represents the signal and background processes considered, $j$ each systematic uncertainty considered, and $i$ each bin of the Monte Carlo templates used for the fit [10]. Also, $\alpha_k$ is the normalization parameter and ultimately what we try to measure by maximizing the likelihood distributions. When we extract the cross sections of the main processes simultaneously, $\alpha_k$ is allowed to float for the signal processes while the background processes have this value fixed at 1. When the individual signal cross sections are extracted, $\alpha_k$ is allowed to float only for the signal process being measured while the other two signal processes and the background samples are fixed at a value

of 1. The number of expected events for each process $k$ in the $i$-th bin is given by $(N_k^{exp})_i$. Each systematic $j$ is given by the fractional uncertainty $f_k$ for each process $k$ where the systematics considered are the same as those discussed in Section 6.6. The only exception to this is that when a cross section for a process is being measured, the systematic uncertainty on that cross section does not contribute since the cross section is what we are attempting to measure.

The systematics themselves are allowed to float in the fit. This is done by using the floating $S_j$ parameters, which are constrained by a Gaussian function centered on zero with a width of one in the likelihood. Because $S_j$ is multiplied by the $f_k$ systematic fractional uncertainty for each process $k$, the systematics in the likelihood are correlated across all bin and processes.

The likelihood $\mathcal{L}$ is a product of the Poisson probabilities over all $i$ bins, also multiplied by the product of the Gaussian constraints on the $j$ systematic uncertainties and given by

$$\mathcal{L} = \left( \prod_i \frac{\mu_i^{n_i} e^{-\mu_i}}{n_i!} \right) \cdot \prod_j e^{\frac{S_j^2}{2}} \tag{13}$$

After maximizing this likelihood, we get a fractional value for $\alpha$ for whatever cross section is being measured [10]. This value is taken as the ratio of the measured cross section for a given process to the the theoretical cross section inputted for that process. Multiplying this fractional value $\alpha$ by the theoretical cross section therefore gives us our measured cross section. In addition to $\alpha$, the likelihood function is also maximized with respect to $S_j$, which also gives an error on the cross section ratio. When multiplied by the theoretical cross section, we obtain a combined systematic and statistical uncertainty on our cross section measurement.

## 6.5 Pseudo Experiments

The signal processes analyzed are $t\bar{t}$, $WW$, and $Z \rightarrow \tau\tau$. First, we get the expected number for the signal and background processes using Monte Carlo sets. The errors for these expected numbers include the statistical, systematic, and luminosity errors. Therefore, we have $N_k^{exp} \pm \Delta N_k^{exp}$ for each process $k$. Recalling the discussion from the Maximum Likelihood section, $\Delta N_k^{exp}$ is equal to the compilation of $f_k^j$ fractional uncertainties for all $j$ while $N_k^{exp}$ is the expected number for a given process over all bins in the two-dimensional phase space of either the $\not\!\!E_T$ vs. $N_{jets}$ or the $\not\!\!E_T$ vs. $\sum E_T$(jets) templates.

Using this expected number and error, a Gaussian distribution is constructed with $< N_k^{exp} >$ as the mean and $\Delta N_k^{exp}$ as one standard deviation. A pseudo-experiment, which is a simulation of a typical data experiment, is constructed by randomly picking some $G_k$ from this Gaussian distribution. This number, obtained by the Gaussian fluctuation is given by

$$G_k = N_k^{exp} \prod_j (1 + f_k^j g_j) \tag{14}$$

where $g_j$ is some random number with a selection probability given by a Gaussian distribution with mean 0 and width of 1. This allows for a correlation for the systematic uncertainties for all considered processes. As well, $G_k$ is the new mean and expected number for only this pseudo-experiment.

Next, we Poisson fluctuate $G_k$ to get $P_k$ which gives the number of events for this particular pseudo-experiment. The number of events differs from the expected number of events because it is an integer. We now have the result $P_k$ for one pseudo-experiment, arising from the expected numbers in the $\not\!\!E_T$ vs. $N_{jets}$ or the $\not\!\!E_T$ vs. $\sum E_T$(jets) templates. The pseudo experiment is then run through the minimization program as if it were data. We repeat this process many more times (e.g. 10,000) in order to

simulate typical data experiments. This pseudo-experiment process is repeated for all signal samples and for the compilation of the background samples. Cross section ratio results for these pseudo-experiments are shown in Figure 8. The curve labeled as the "true value" in this figure is the number of events generated for a given process divided by the nominal prediction (from the Monte Carlos expectations) while the "measured value" is the value of the cross section returned by the fit divided by the inputted theoretical cross section value.

An example of the measured positive and negative errors (including statistical, systematic, and luminosity uncertainties) are shown in Figure 9.

In order to test if our pseudo-experiments are modeling the data correctly, we use pull distributions, which show whether we are possibly overestimating or underestimating the data. A correct estimation and validation of our pseudo experiment procedure will yield a distribution that is Gaussian-like, with a mean of 0 and width of 1. For asymmetric errors, the pull distributions are defined as

$$g = \begin{cases} \frac{\tau_g - \tau_m}{|\sigma_m^+|} & \text{for } \tau_m \leq \tau_g \\ \frac{\tau_m - \tau_g}{|\sigma_m^-|} & \text{for } \tau_m > \tau_g \end{cases} \tag{15}$$

where $\tau_g$ is the generated value from the fit, $\tau_m$ is the measured value (discussed above), and $\sigma_m^{\pm}$ are the positive and negative errors on our measured values. An example of a pull distribution from our pseudo experiments are shown in Figure 10

## 6.6 Systematics

We have two classes of systematics that we treat differently in our analysis, one, the systematic uncertainty (from various sources) on the acceptances themselves, and a second due to the effect on the fitted cross sections from changes in the $\not\!\!E_T$-$N_{jet}$ shapes due to various sources. The following 2 subsections give a brief overview of our two

systematic sources.

### 6.6.1 Acceptance systematics

A summary of our acceptance systematics is given in Table 6.6.1. We incorporate these systematics in our fit by allowing the acceptances to vary in the likelihood function within a Gaussian constraint (of width given by the systematic error) as discussed in Section 6.4. In addition, although not explicitly mentioned above, we have a similar Gaussian constraint for the luminosity (of width 5.9%).

| | $t\bar{t}$ | $WW$ | $Z \to \tau\tau$ |
|---|---|---|---|
| Lepton ID | 1.9 % | 1.9 % | 1.9 % |
| Trigger Eff. | 2.1 % | 2.2 % | 3.5 % |
| MC Dependence | 4.1 % | 3.5 % | – |
| Process Cross Section | 10.0 % | 10.0 % | 5.0 % |

Table 16: Summary of systematic uncertainties on the acceptance for each "signal" process.

| | $Z \to ee$ | $Z \to \mu\mu$ | $ZZ$ | $WZ$ | $W\gamma$ | $W + jets$ |
|---|---|---|---|---|---|---|
| lepton ID | 1.9 % | 1.9 % | 1.9 % | 1.9 % | 1.9 % | 1.9 % |
| Trigger Eff. | 3.5 % | 3.5 % | 3.5 % | 3.5 % | 3.5 % | 3.5 % |
| Process Cross Section | 5.0 % | 5.0 % | 10.0 % | 10.0 % | 10.0 % | – |
| Fakes | – | – | – | – | – | 28.6 % |

Table 17: Summary of systematic uncertainties on the acceptance for each "background" process.

### 6.6.2 Shape systematics

We investigated the effect of sources of uncertainties on the shapes of the $\not\!\!E_T$ vs. $N_{jets}$ distributions. These include Jet Energy Scale, ISR and FSR, and the effect of different bin sizes [2].

- **Jet Energy Scale :** Because a jet is the result of many particles traversing through the detector, it is harder to estimate the energy of them than a single particle track. Therefore, to see what kind of difference a jet energy mismeasurement might make we use pseudo-experiments sampled from templates created from increasing and decreasing the jet energies by 10% (a large overestimate of our JES systematic), we found the effect on the expected cross sections to vary by about 2% for $WW$ and $Z \to \tau\tau$, and about 5% for $t\bar{t}$. Given that the actual JES systematic varies between about 2% and 3% the shape systematic due to this effect is probably a couple of percent at most.

- **ISR/FSR :** To estimate this effect we used standard samples of more/less ISR/FSR (coming from gluons that radiate from the initial or final state interactions). In all cases the effect on the cross sections was around 2% or less. This effect will also be correlated to the JES effect.

- **Bin size:** To estimate the effect of bin size, we halved the bin size (doubled the number of bins) in the $\not\!\!E_T$-$N_{jet}$ fits. The effect on the mean cross section from pseudoexperiments was negligible (less than 1%).

The conclusion is that these effects are small compared to our acceptance systematics, the total being of order 3% (as an upper limit) for all signal processes. We therefore do not include a separate shape systematic in our quoted results.

## 6.7 The Data Events and Grand Summary Table of the Standard Model Expectations

### 6.7.1 Grand Summary Table

Table 18 shows the summary of all the signal and background expectations discussed in the previous sections. The luminosity normalised to for each process depends slightly on that process but on average is $184 \pm 11\,\mathrm{pb}^{-1}$. The errors include statistical and systematics on the acceptances. Also shown are the number of observed events in each channel from our data samples [2].

| | $e\mu$ Final State |
|---|---|
| Signal Processes | |
| $t\bar{t}$ | 82.4 ± 10.4 |
| $WW$ | 128.0 ± 16.2 |
| $Z \to \tau\tau$ | 470.6 ± 40.9 |
| Background Processes | |
| $DY \to ee$ | 0.19 ± 0.02 |
| $DY \to \mu\mu$ | 102.9 ± 17.6 |
| $WZ$ | 4.6 ± 0.6 |
| $ZZ$ | 1.0 ± 0.1 |
| $W\gamma$ | 12.0 ± 1.6 |
| $W + fake\ lepton$ | 52.5 ± 21.3 |
| Total expected MC Event Count | 854 ± 88 |
| Data | 781 |

Table 18: Numbers of Expected Events

### 6.7.2 $\not\!\!E_T$ vs. $N_{jet}$ Jets Distributions

The $\not\!\!E_T$-$N_{jet}$ and $\not\!\!E_T$-$\sum E_T(jets)$ 2-D parameter space distributions for the expected signal processes, and the "fixed" total background as well as theshapes that are fit to the corresponding data distribution for the cross section extractions of the signal processes are shown in Figures 11, 12, 13, 14.

# 7 Cross Section Results

We fit the data to our Standard Model signal templates using the scenarios discussed earlier and which are all summarized in Tables 19 and 20.

| | $e\mu$ Final State | Theory |
|---|---|---|
| $\not\!\!E_T$ vs. $N_{jets}$ | | |
| $\sigma(t\bar{t})$ ($WW$ and $Z \to \tau\tau$ Constrained) | $8.20^{+1.04}_{-0.98}(\text{Stat})^{+0.54}_{-0.43}(\text{Syst})$ pb | 6.7 pb |
| $\sigma(WW)$ ($t\bar{t}$ and $Z \to \tau\tau$ Constrained) | $12.28^{+1.75}_{-1.65}(\text{Stat})^{+1.07}_{-0.88}(\text{Syst})$ pb | 12.4 pb |
| $\sigma(Z \to \tau\tau)$ ($t\bar{t}$ and $WW$ Constrained) | $1513\ ^{+94}_{-91}(\text{Stat})^{+145}_{-130}(\text{Syst})$ pb | 1780.8 pb |
| $\not\!\!E_T$ vs. $\sum E_T(\text{jets})$ | | |
| $\sigma(t\bar{t})$ ($WW$ and $Z \to \tau\tau$ Constrained) | $7.41^{+1.02}_{-0.95}(\text{Stat})^{+0.41}_{-0.34}(\text{Syst})$ pb | 6.7 pb |
| $\sigma(WW)$ ($t\bar{t}$ and $Z \to \tau\tau$ Constrained) | $13.19^{+1.84}_{-1.73}(\text{Stat})^{+1.13}_{-0.94}(\text{Syst})$ pb | 12.4 pb |
| $\sigma(Z \to \tau\tau)$ ($t\bar{t}$ and $WW$ Constrained) | $1464^{+91}_{-88}(\text{Stat})^{+145}_{-130}(\text{Syst})$ pb | 1780.8 pb |

Table 19: Extracted cross sections with only one signal process floating while the other two signal processes and all backgrounds are constrained within their Gaussian uncertainties

| | $e\mu$ Final State | Theory |
|---|---|---|
| $\not\!\!E_T$ vs. $N_{jets}$ | | |
| $t\bar{t}$ | $7.81^{+0.99}_{-0.93}(\text{Stat})^{+0.71}_{-0.55}(\text{Syst})$ pb | 6.7 pb |
| $WW$ | $11.66^{+1.46}_{-1.37}(\text{Stat})^{+1.65}_{-1.42}(\text{Syst})$ pb | 12.4 pb |
| $Z \to \tau\ tau$ | $1542^{+97}_{-95}(\text{Stat})^{+175}_{-154}(\text{Syst})$ pb | 1780.8 pb |
| $\not\!\!E_T$ vs. $\sum E_T(\text{jets})$ | | |
| $t\bar{t}$ | $6.70^{+0.91}_{-0.85}(\text{Stat})^{+0.64}_{-0.51}(\text{Syst})$ pb | 6.7 pb |
| $WW$ | $11.87^{+1.62}_{-1.53}(\text{Stat})^{+1.58}_{-1.32}(\text{Syst})$ pb | 12.4 pb |
| $Z \to \tau\tau$ | $1451^{+92}_{-90}(\text{Stat})^{+172}_{-152}(\text{Syst})$ pb | 1780.8 pb |

Table 20: Extracted cross sections with all three signal process floating while all backgrounds are constrained within their Gaussian uncertainties

# 8 Likelihood of Standard Model hypothesis

The fit results to the entire parameter space(s) yield likelihood values consistent with that from pseudo-experiments [2]. This are shown in Figures 15 and 16.

However, this is not necessarily a very good measure of the consistency to the SM as it might not be sensitive to significant variations in regions with relatively low statistics. We therefore split the $\not\!\!E_T$ vs. $N_{jet}$ parameter space into 4 regions like so (we do this only for the $\not\!\!E_T$ vs. $N_{jet}$ parameter space as these represent our main results):

- region 1: $\not\!\!E_T < 20\ GeV$, $N_{jets} \leq 1$ ($Z \to \tau\tau$ and backgrounds expected here)
- region 2: $\not\!\!E_T > 20\ GeV$, $N_{jets} \leq 1$ ($WW$ expected here)
- region 3: $\not\!\!E_T > 20\ GeV$, $N_{jets} \geq 2$ ($t\bar{t}$ expected here)
- region 4: $\not\!\!E_T < 20\ GeV$, $N_{jets} \geq 2$ (no significant contributions from signal processes expected here)

Table 21 summarizes the results from comparing the likelihood from the data to pseudo-experiments in each of these regions. The corresponding likelihood plots are given in Figure 17.

| | |
|---|---|
| Region 1 | 86.7% |
| Region 2 | 25.1% |
| Region 3 | 24.8% |
| Region 4 | 32.2% |

Table 21: Percentage of pseudo-experiments with a likelihood greater than that from the fit to the data for each of the 4 regions in the $\not\!\!E_T$ vs. $N_{jet}$ parameter space. The fit is that with all three signal processes floating.

# 9 Conclusions

Due to the nice separation of our main processes in the $\not\!\!E_T$-$N_{jet}$ and $\not\!\!E_T$ vs. $\sum E_T$(jets) and simultaneous extraction of their cross sections, this analysis gives us a more global test of the SM using dilepton events than a dedicated cross section measurement, and we quantify the consistency of the our data in various regions of the $\not\!\!E_T$-$N_{jet}$ parameter space.

This could be used for more specific searches for new physics, and we plan on developing this using same-sign dileptons events, and as a tool for looking at early data at the Large Hadron Collider at CERN.

# References


[1] C. Amsler *et al. Physics Letters, B667(1), 2008.*

[2] M. Stephen M. Smith, D. Benjamin, M. Kruse, D. Hidas "An Inclusive Dilepton Analysis using 3 $fb^{-1}$", CDF-note 9733.

[3] Dean Andrew Hidas. "Search for Standard Model Higgs Bosons Decaying to W-Boson Pairs in $p\bar{p}$ Collisions at $\sqrt{s}$=1.96 TeV". Doctoral Thesis. Duke University Department of Physics. 2008.

[4] Sebastian Carron Montero. "Measurement of the $t\bar{t}$, $WW$, $Z \rightarrow \tau\tau$ Production Cross Sections in $p\bar{p}$ Collisions at $\sqrt{s}$=1.96 TeV". Doctoral Thesis. Duke University Department of Physics. 2006.

[5] HWW main note.

A. Abulencia *et al.* (CDF collaboration), "Search for Higgs Bosons decaying to pairs of $W$-Bosons", Phys. Rev. Lett. 102, 021802 (2009). arXiv:0809.3930

[6] The Particle Data Group. http://pdg.lbl.gov.

[7] Top Group Monte Carlo "TopNtuples". http://www-cdf.fnal.gov/internal/physics/top/RunIIMC/topmc6/.

[8] The Collider Detector at Fermilab (CDF). www-cdf.fnal.gov.

[9] F. James, Minuit Reference Manual, Version 94.1. http://wwwasdoc.web.cern.ch/wwwasdoc/WWW/minuit/minmain/minmain.html.

[10] CDF-8128, Tom Junk

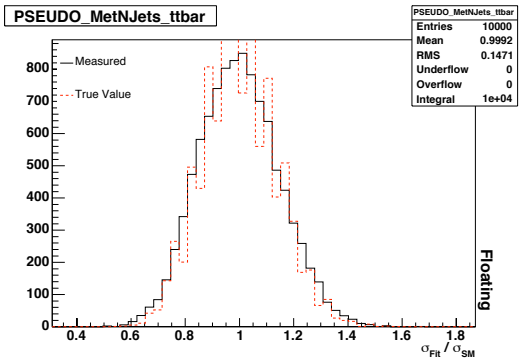


(a) $\not\!\!E_T$ vs. $N_{jets}$

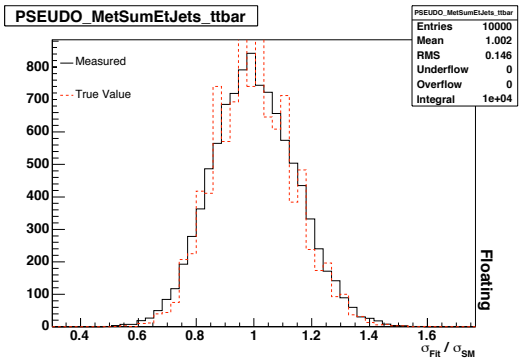


(b) $\not\!\!E_T$ vs. $\sum E_T$(jets)

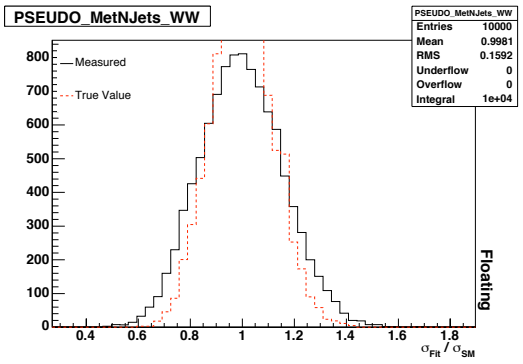


(c) $\not\!\!E_T$ vs. $N_{jets}$

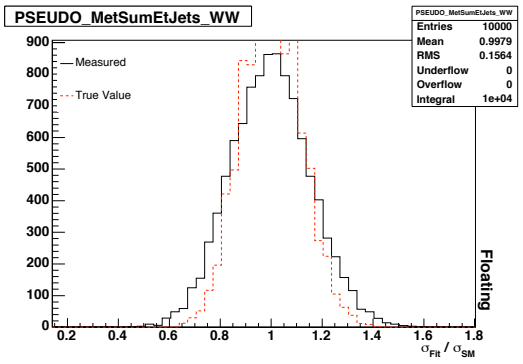


(d) $\not\!\!E_T$ vs. $\sum E_T$(jets)

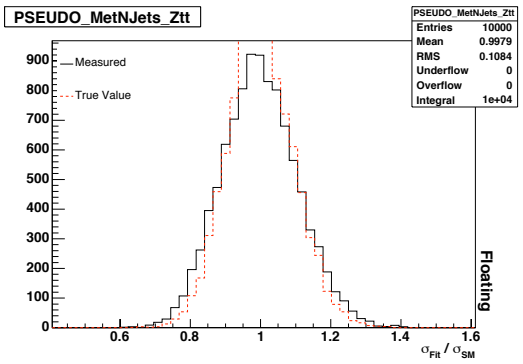


(e) $\not\!\!E_T$ vs. $N_{jets}$

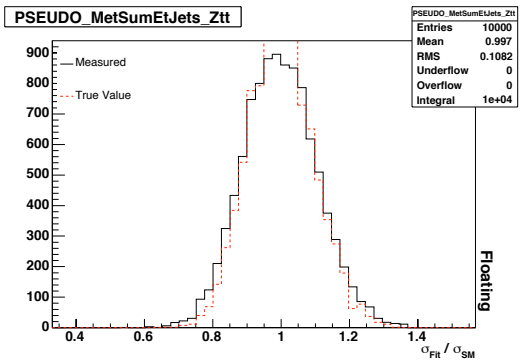


(f) $\not\!\!E_T$ vs. $\sum E_T$(jets)

Figure 8: Cross section ratio plots for signal samples from pseudo-experiments using $\not\!\!E_T$ vs. $N_{jets}$ and $\not\!\!E_T$ vs. $\sum E_T$(jets) templates.

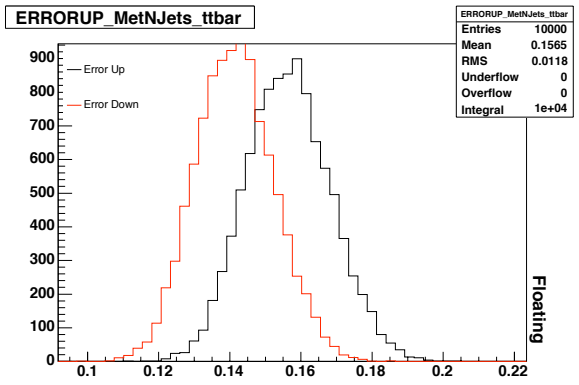


Figure 9: Measured errors in pseudo experiments for $t\bar{t}$ (from $\not\!\!E_T$ vs. $N_{jets}$ templates.

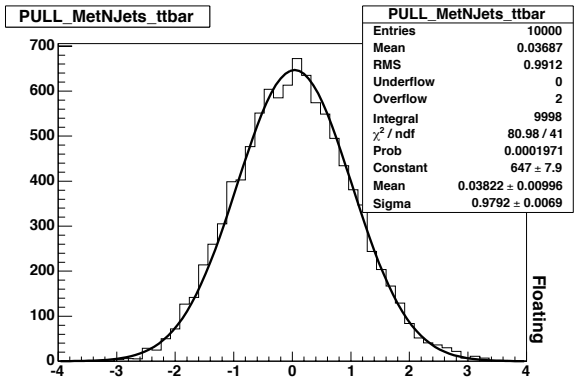


Figure 10: Pull distribution for $t\bar{t}$ (from $\not\!\!E_T$ vs. $N_{jets}$ templates.

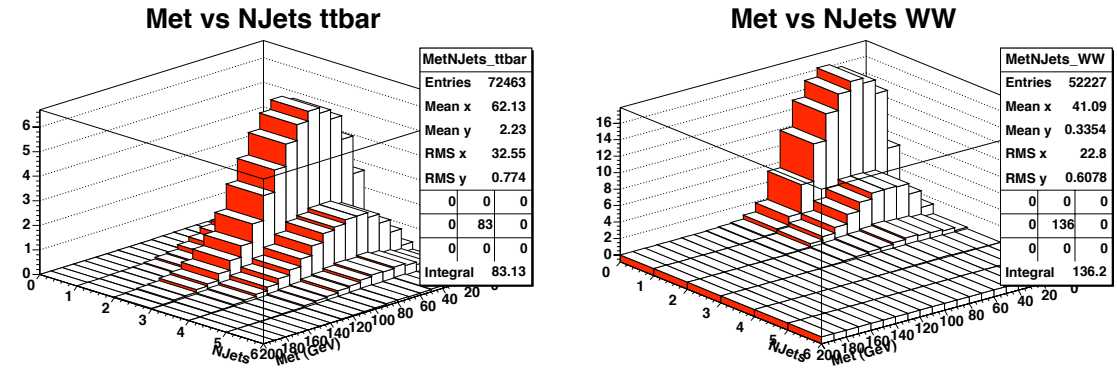


(a) $t\bar{t}$ Process




(b) $WW$ Process

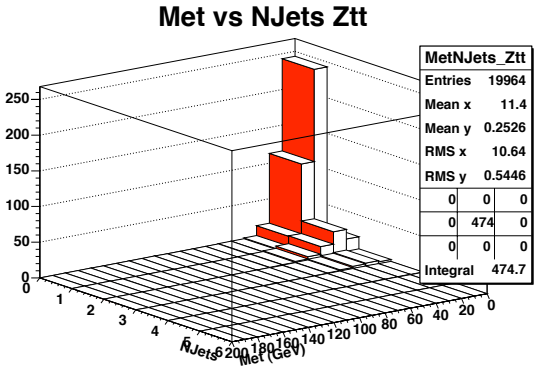


(c) $Z \rightarrow \tau\tau$ Process

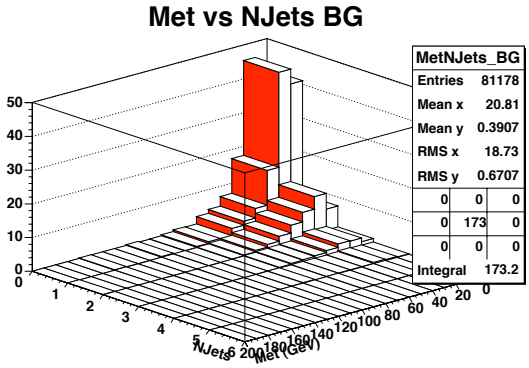


(d) Background Processes

Figure 11: $\not\!\!E_T$ vs. $N_{jets}$ templates created from Monte Carlo samples.

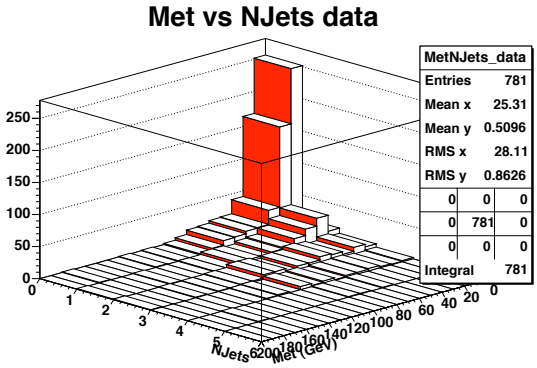


(a) Data (Linear Scale)

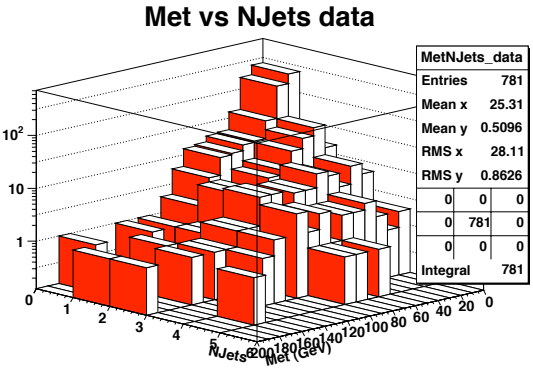


(b) Data (Logarithmic Scale)

Figure 12: $\not\!\!E_T$ vs. $N_{jets}$ templates for the data used in this analysis.

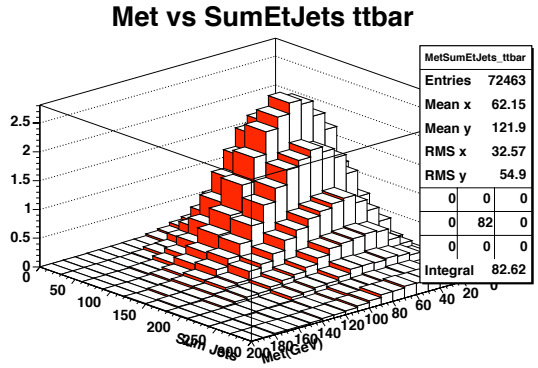


(a) $t\bar{t}$ Process

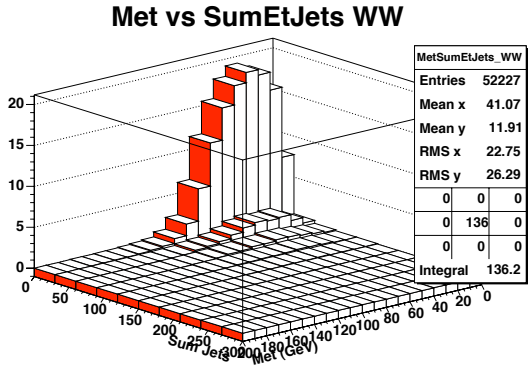


(b) $WW$ Process

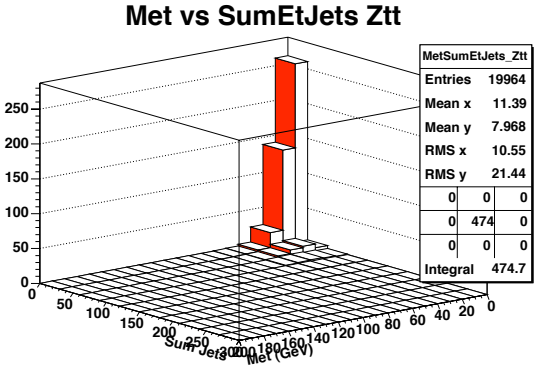


(c) $Z \rightarrow \tau\tau$ Process

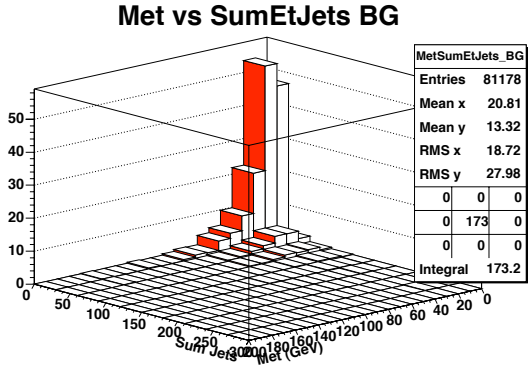


(d) Background Processes

Figure 13: $\not\!\!E_T$ vs. $\sum E_T$(jets) templates created from Monte Carlo samples.

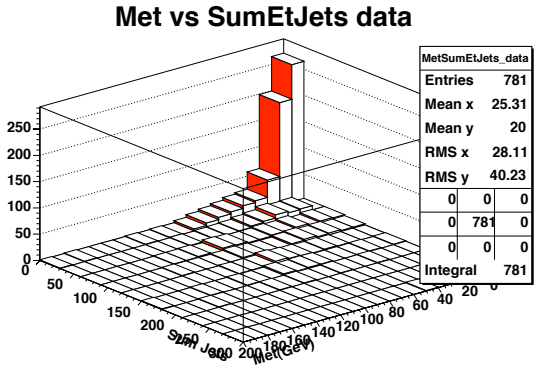


(a) Data (Linear Scale)

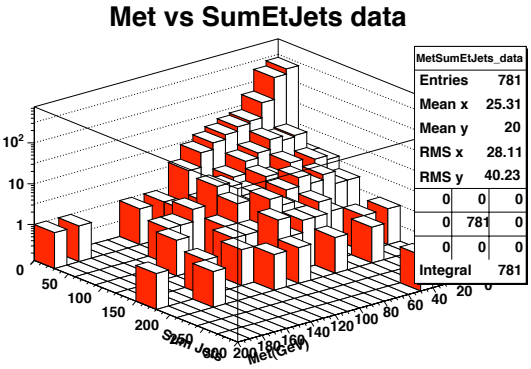


(b) Data (Logarithmic Scale)

Figure 14: $\not\!\!E_T$ vs. $\sum E_T$(jets) templates for the data used in this analysis.

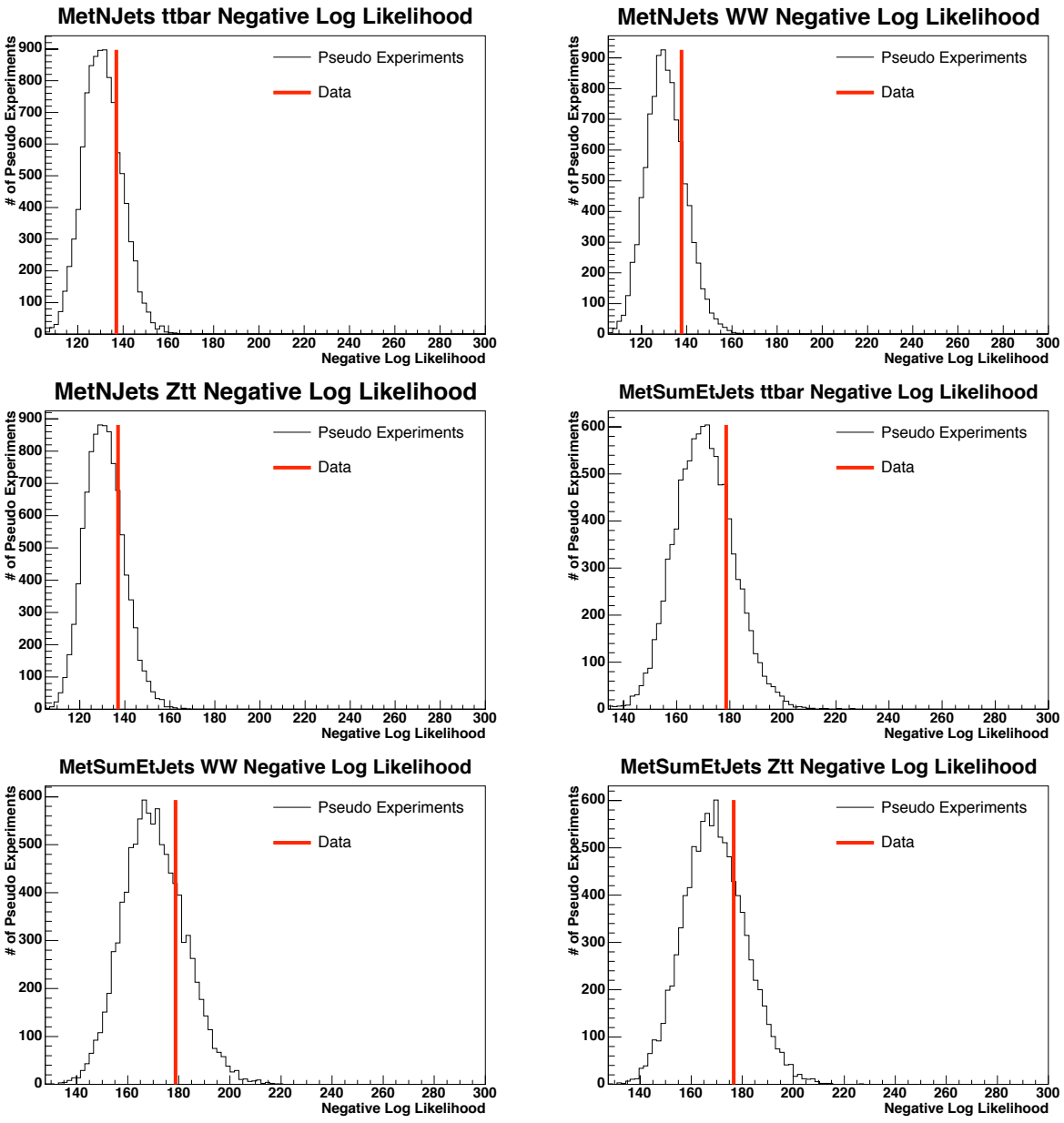


Figure 15: Negative log-likelihood values from fits to the data (solid red line) as compared to the distributions from pseudo-experiments. These correspond to the fits where all but the measured process is constrained in the fit, for fits using the both the $\not\!\!E_T$ vs. $N_{jet}$ and $\not\!\!E_T$ vs. $\sum E_T(jets)$ parameter spaces.

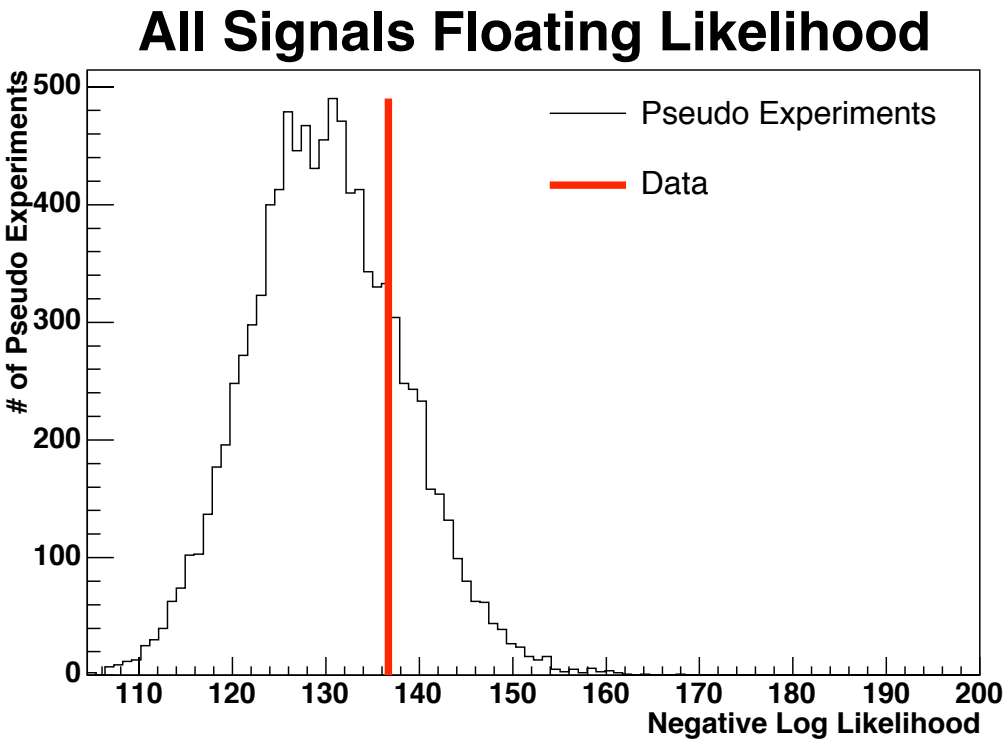


Figure 16: Negative log-likelihood value from the $\not\!\!E_T$-$N_{jet}$ fit to the data with all signal processes floating (solid red line) as compared to the distribution from pseudo-experiments.

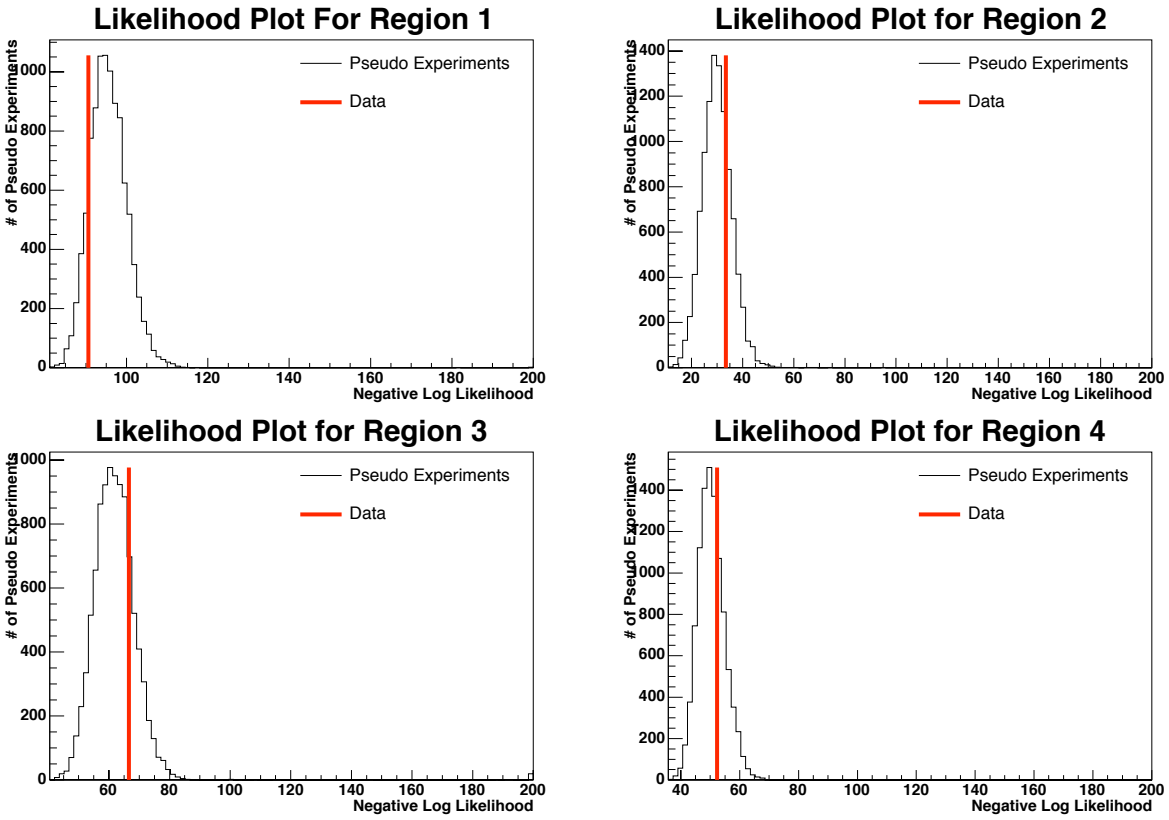


Figure 17: Negative log-likelihood values from the $\not\!\!E_T$-$N_{jet}$ fits to the data with all signal processes floating (solid red line) as compared to the distributions from pseudo-experiments, for the four regions discussed in the text.